Contents

Introduction

The interaction of condensed matter with the external environment occurs at surfaces. Usually, a solid surface modifies the electronic properties of the atoms and/or molecules which bind to it: at the same time, the adsorbates can modify the structural and electronic properties of the surface [1]. Recently, transition metal surfaces have attracted a wide scientific and technological interest because of their capability of reducing the activation energy barrier for many important chemical reactions [2]. An example is the formation of water from molecular oxygen and hydrogen in the presence of a platinum surface. In order to form an H_2O molecule, H_2 and O_2 must first transform to atoms. The energy needed for this atomization to occur is 4.48 and 5.08 eV for H_2 and O_2 respectively [3], so it is very improbable that the molecules break at room temperature. The presence of the platinum surface reduces these energy barriers. Actually, at the surface the molecules spontaneously dissociate and the reaction occurs explosively.

Among transition metal surfaces, rhodium and platinum are two of the most studied because they have been demonstrated to be the best catalysts for the reaction $2CO + 2NO \rightarrow 2CO_2 + N_2$. This reaction is particularly important because it eliminates the two poisonous CO and NO gases from the combustion engines exhaust gas. A powdered mixture of rhodium and platinum is actually used in the automobile's catalytic devices.

Most transition metals have a cubic crystal geometry. The most widely studied surfaces are those with low Miller indices, such as (111), (001), and (110). The latter is particularly interesting in the case of the FCC transition metals (Cu, Pd, Au, Ni, Pt, etc.), because the energy difference between the unreconstructed (1×1) surfaces and the reconstructed $(1 \times n), n = 1, 2, 3, 5, ...$, missing- or added-row [1] ones is small [4, 5]. For example, for Au, Pt, and Ir the (1×2) state is the more stable. Molecular adsorption can modify the energetic balance and induce a transition from a $(1 \times n)$ state towards a $(1 \times m)$ state, where n and m are two different missing- or added-row reconstruction indices [6]. This is the case for rhodium, which has a (1×1) stable structure, but it undergoes an added-row reconstruction upon oxygen adsorption [6, 7, 8]. These reconstructed surfaces are meta-stable upon elimination of oxygen by exposition to H_2 or CO. To re-obtain the unreconstructed (1×1) surface it is sufficient to anneal the rhodium surface above 480^o K.

In order to understand the mechanism of a surface chemical reaction, a detailed knowledge of the adsorption geometries for the atoms or the molecules involved is required. These reactions involve the modification of the atomic electronic clouds and therefore a quantum mechanical description of the corresponding processes is necessary. A direct solution of the many-body Schrödinger equation for a surface is a formidable task. A good compromise between accuracy of the results and reasonable computational effort is given by the *Density Functional Theory* (DFT) within the *Local Density Approximations* (LDA) and its gradient-corrected generalizations [9, 10]. A further approximation which usually does not introduce additional significant loss of accuracy is the *pseudopotential* one, where essentially one disregards the tightly bound atomic core electrons which do not participate in the chemical bonds among the atoms and are difficult to treat.

The development of these efficient theoretical *first principles* techniques along with the availability of faster and faster computational resources has allowed, during the past 30 years, the investigation of real systems of increasing size and complexity. The reliability of DFT calculations in describing the structural and vibrational properties of simple materials has been demonstrated by the successful and thorough

[1] A missing-(added-)row $(1 \times n)$ reconstruction is a surface where for every n rows one is missing (added).

comparison with a great deal of experimental data. Moreover, they are unbiased from any external prejudice and therefore they are very general tools. The main power of *first principles* is maybe the capability to explore physical properties that are inaccessible to experiments, and therefore they are in a sense complementary to them. For example one has a direct control onto the atomic positions, and can relate the structural properties to the electronic ones, as the electronic charge transfer during the formation of the chemical bonds. Also, one can calculate the forces on the atoms to find the equilibrium configurations, or use the forces to study the dynamical evolution of the system (see for example Ref. [11] for a discussion on the applications of DFT). All these facts make DFT a unique technique to study all those systems where a quantum mechanical description of the processes is necessary.

Motivated by a collaboration with an experimental group working at the *Elettra* synchrotron-radiation facility in Trieste [12], we decided to apply state-of-the-art density-functional techniques to the study of some physical and chemical properties of the (110) and the (001) surfaces of rhodium upon carbon-monoxide and oxygen adsorption respectively.

The adsorption of CO molecules on the (110) surface of rhodium has been studied experimentally by means of a variety of techniques [13, 14, 15, 16, 17, 18, 19, 20, 21]. Using LEED (Low Energy Electron Diffraction), for example, one gets information about the reciprocal surface lattice, i.e. one can determine the periodicity of the surface. Furthermore, if the intensity of the spots in the LEED pattern is analyzed as a function of the electrons energy (LEED I-V), it is also possible to obtain some information on the real-space structure of the surface lattice. A LEED I-V analysis of the adsorption of 1 monolayer (ML) of carbon monoxide on the unreconstructed surface results in a (2×1)p2mg structure, with the C atom bound in the short bridge sites along the $(1\bar{1}0)$ direction, and the molecular axis alternatively tilted with respect to the surface normal, towards (001) direction [18]. The axis which connects the center of the bridge site and the carbon atom of the molecule is also tilted in the same fashion. The same geometry is also observed on the (110) surfaces of Ir, Ni, Pd, and Pt [22, 23, 24, 25]. On Ni(110) [26] and Pd(110) [27] the adsorption sites are respectively *bridge* and *on-top*. The tilt angles of the CO molecules also depend on the metal they are adsorbed on. In particular, the smaller is the lattice parameter—Ni(2.48 Å) < Rh(2.69 Å) < Pd(2.74 Å)—the larger is the metal-C angle [18], i.e. the larger is the molecule-molecule distance because the molecules are alternatively tilted. This fact suggests that the mechanism responsible for the tilt is the molecule-molecule interaction. However, the same trend is not observed for the tilt of the C-O axis, which is minimum for palladium and maximum for rhodium.

The finite temperature properties of these systems are particularly interesting. Using the TPD (Temperature Programmed Desorption) technique one obtains information on the adsorption energies and one can possibly distinguish among different species of adsorbates which bind to the surface with different energies. In Ref. [15], the (2×1)p2mg LEED pattern was reported to disappear at temperatures higher than $\approx 270 \div 280$ °K, well below the desorption of CO from the surface, which starts at temperature above $\approx 350 \div 360$ °K. This fact was tentatively explained in terms of an order-disorder phase-transition.

CO adsorption on the (110) surface of various transition metals does not change the substrate surface ordering. On rhodium, for example, the only appreciable effect it has on the substrate is to reduce the relaxation of the first surface layer from $\approx -10\%$ of the clean surface to $\approx +2\%$ for the CO covered one.

If we consider the (001) surface of some transition metals, in particular rhodium and nickel, further adsorbate-induced effects are observed. Oxygen adsorption on Rh(001) is known to be dissociative and to saturate at half a monolayer, independently on the adsorption temperature. At this coverage a 2×2 reconstruction has been observed by LEED studies and confirmed by STM images [28]. STM (Scanning Tunnel Microscopy) is a real space technique which allows a direct observation of the surface. This technique is very powerful, but it can be misleading. The obtained images do *not* represent the surface atoms but rather their local density of states

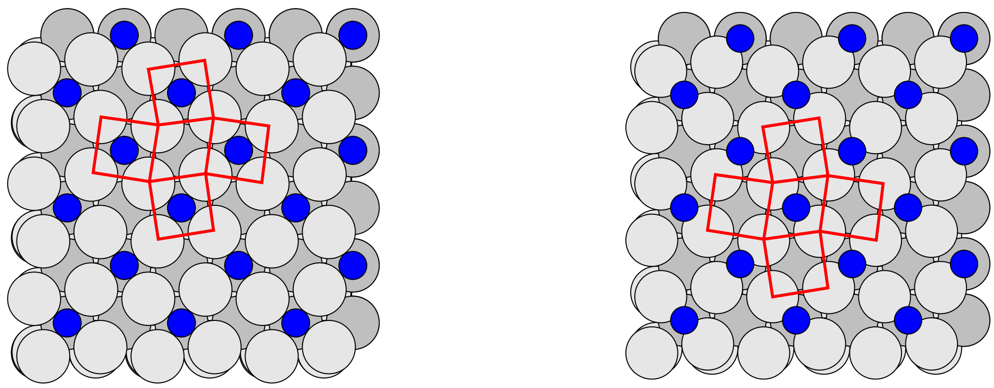

(a) 'black' (b) 'white'

Figure 0.1: (Color) The two possible reconstructions compatible with LEED and STM data of Ref. [28]. In (a) we display the 'black' reconstruction while in (b) the 'white' one.

(DOS) at the Fermi energy. If a particular atom has low DOS near the Fermi level, then it can be "invisible". This is what occurs, for example, for carbon, nitrogen, and oxygen adsorbed on the (001) surface of rhodium and nickel.

On the Rh(001) surface the oxygen atoms sit in the troughs formed by four first-layer rhodium atoms and fill the sites in a $c(2 \times 2)$ geometry. This geometry may be seen as a chess-board whose 'black' squares are occupied by oxygen atoms, while the 'white' ones are empty. Within this picture, the reconstruction observed in Ref. [28] can be described as a clockwise and counterclockwise rotation of the 'black' or the 'white' squares, resulting in a (2×2)p4g symmetry (see Fig. 0.1). This distortion preserves the shape of the 'black' squares, while the 'white' ones become rhomboid (or vice-versa). A similar behavior is observed for nitrogen and carbon adsorbed on the (001) surface of nickel, where the rotation angle of the squares is much larger, and the reconstruction is therefore more evident [29, 30, 31, 32]. From LEED and STM analysis it is not possible to decide if it is the 'black' or the 'white' squares which rotate. The oxygen atoms form a square lattice with side length $\sqrt{2}$ times the substrate side length and 45° rotated with respect to the chess-board.

What characterizes the two reconstructions is the position of the oxygen over-layer with respect to the substrate, which is identical in the two cases. Looking only at the reciprocal lattice image (LEED) it is not possible to decide to which of the two reconstructions it corresponds. Using STM is possible to see the reconstructed substrate only if the oxygen atoms are "invisible", otherwise only the oxygen over-layer is imaged. Therefore not even STM is capable to distinguish between the two possibilities. However, additional experimental data exist for C/Ni(001) (LEED I-V) [32] and N/Ni(001) (SEXAFS) [33] which allow a more precise characterization of the reconstruction, and in these two cases it is observed that it is the 'black' (occupied) squares which rotate. In analogy with these two systems, in Ref. [28] the same type of reconstruction was proposed also for O/Rh(001). However, even if these three systems seem to behave in a very similar manner, there is a non-negligible difference between O/Rh(001) and C,N/Ni(001). While nitrogen and carbon penetrate into the substrate when adsorb on Ni(001), becoming essentially *five-fold* coordinated, the same behaviour is not observed for the O/Rh(001) system, where the oxygen atoms stay relatively far from the plane of the site. Therefore, while in the case of C and N the surface site must enlarge in order to accommodate the adsorbed atoms, and the enlargement results in a 'black' reconstruction, this is not the case in the O/Rh(001) case, where there is no need of site enlargement at all.

In this thesis we report on a *first principles* investigation of some structural and electronic properties of the (110) and (001) surfaces of rhodium upon carbon-monoxide and oxygen adsorption respectively.

The structure and phase stability of one ML of CO molecules adsorbed on the Rh(110) (1×1) surface are studied from first principles and by mapping the low-lying energy configurations corresponding to the different distributions of tilt angles onto an anisotropic 2D spin model. The ground-state structure of the system is determined by means of accurate structure minimizations, and the finite temperature properties are studied using a standard Metropolis Monte Carlo simulation on the spin model.

Then, we present a (*ab-initio*) study of the oxygen adsorption on the Rh(001) surface. At variance with the proposal of Ref. [28] we find that it is the 'white' squares which rotate rather then the 'black' ones. The reconstruction mechanism is explained using simple chemical concepts based on the atomic orbitals involved in the rhodium-oxygen bond. Finally, we present some preliminary results for related systems C, N, and O adsorbed on Ni(001).

The thesis is organized as follows. The first chapter contains a review of the fundamental theoretical tools used in the *first principles* calculations. The second chapter contains our theoretical results. Finally, we present our conclusions. Some technical questions are discussed in the Appendices.

Chapter 1

Theoretical tools

The calculations presented in this thesis are performed using *Density Functional Theory* for the ground-state (GS) structural and electronic properties, and Metropolis Monte Carlo simulations to study the finite temperature behaviour, where needed.

The investigation of the microscopic properties of matter is a very complicated task. One has to solve the Schrödinger equation of the system,

$$H\Psi \;=\; E\Psi. \tag{1.1}$$

The systems in which we are interested in are formed by ions, say M, with charge Z_j and mass M_j, and electrons, say N. In the non-relativistic approximation, the Hamiltonian appearing in Eq. 1.1 reads:

$$\begin{aligned} H \;=\; & \sum_{i=1}^{N}(-\frac{1}{2}\nabla^2_{\mathbf{r}_i}) \;+\; \sum_{j=1}^{M}(-\frac{1}{2M_j}\nabla^2_{\mathbf{R}_j}) \;+ \\ & - \sum_{i=1}^{N}\sum_{j=1}^{M}\frac{Z_j}{|\mathbf{r}_i - \mathbf{R}_j|} \;+\; \sum_{i<j}^{N}\frac{1}{r_{ij}} \;+\; \sum_{i<j}^{M}\frac{Z_iZ_j}{R_{ij}}, \end{aligned} \tag{1.2}$$

where atomic units have been used ($e^2 = m_e = \hbar = 1$). This equation is in practice impossible to solve and then one needs some reasonable approximations. The first approximation which can be done is the separation of the ionic degrees of freedom from the electronic ones. This is the so called Born-Oppenheimer (or adiabatic) approximation. Ions are much heavier then electrons and then the electrons follow adiabatically the ions movements, remaining close to their instantaneous ground-state. In this way the ions act as external potential source for the electronic problem, which therefore depends parametrically on the ionic positions,

$$
\begin{aligned}
(H\{\mathbf{R}\} - E\{\mathbf{R}\})\psi\{\mathbf{r};\mathbf{R}\} &= 0, \\
H\{\mathbf{R}\} &= \sum_{i=1}^{N}(-\frac{1}{2}\nabla^2_{\mathbf{r}_i}) - \sum_{i=1}^{N}\sum_{j=1}^{M}\frac{Z_j}{|\mathbf{r}_i - \mathbf{R}_j|} + \sum_{i<j}^{N}\frac{1}{r_{ij}}.
\end{aligned}
\tag{1.3}
$$

Once the electronic problem is solved (ideally for each ionic position), the dynamics of the ions can be studied using the electronic energy $E\{\mathbf{R}\}$ as *effective* potential. Usually ions are heavy enough to be treated as classical particles, which is therefore a further reasonably approximation. However, Eq. 1.3 does not seem to be easier to solve then Eq. 1.2 cause to the presence of the two-body term due to electron-electron interaction which couples all the electronic degrees of freedom. Beside the Schrödinger equation, a new formalism has been developed in the last three decades: it is the *Density functional theory* [9, 10], and it overcomes the many-body difficulties providing an alternatively exact new formalism which is much easier to handle.

1.1 Density functional theory

The original idea which started the development of DFT is due to Hohenberg and Kohn (HK) [34]. They showed that the external potential acting on the electrons is uniquely determined (up to a trivial additive constant) by the electron GS density $n(\mathbf{r}) = \langle\Psi|\hat{n}(\mathbf{r})|\Psi\rangle = \int d\mathbf{r}_2 \ldots d\mathbf{r}_n |\Psi(\mathbf{r}, \mathbf{r}_2, \ldots, \mathbf{r}_n)|^2$, where Ψ is the GS of the system and $\hat{n}(\mathbf{r})$ is the density operator. Since $n(\mathbf{r})$ determines also the number of electrons N, and since V_{ext} and N fix the Hamiltonian of the system, it turns out that the electron density completely determines the system.

The energy can be written:

$$
E[n] = F_{HK}[n] + \int V_{ext}(\mathbf{r})n(\mathbf{r})d\mathbf{r}, \tag{1.4}
$$

with

$$
F_{HK}[n] = \langle\Psi_o[n]|T + V_{ee}|\Psi_o[n]\rangle, \tag{1.5}
$$

where T and V_{ee} are respectively the kinetic energy and the electron-electron interaction operators, and $\Psi_o[n]$ is the GS of the system. Note that $F_{HK}[n]$ does not depend on the external potential and therefore it is a universal functional. Using the variational principle HK proved a second theorem which states that the GS density of the system is the one which minimizes $E[n]$, and the minimum of $E[n]$ is the GS energy E_0. It is clear the importance of these two results, the only quantity which is needed is the electron density, no matter how many electrons are present in the system! The exact form of the functional $F[n]$ is not known, however, its existence justifies the large work that is still in progress to improve the approximations available nowadays.

One year after the publication of the HK paper Kohn and Sham (KS) invented an indirect method to solve the problem [35]. The idea is to write the energy functional as an "easy" part plus a "difficult" part.

$$F[n] \; = \; T_0[n] \; + \; E_H[n] \; + \; E_{xc}[n], \tag{1.6}$$

where $T_0[n]$ is the GS kinetic energy of an *auxiliary* non-interacting system whose density is the same as the one of the real system, $E_H[n]$ is the repulsive electrostatic energy of the classical charge distribution $n(\mathbf{r})$ and $E_{xc}[n]$ is the exchange-correlation (XC) energy defined through Eq. 1.6. Minimizing the total energy $E[n]$ under the constraints of orthonormality for the one-particle orbitals of the auxiliary system, $\int \psi_i^*(\mathbf{r})\psi_j(\mathbf{r})d\mathbf{r} \; = \; \delta_{ij}$, one finds a set of one-particle Schrödinger equations:

$$\left[-\frac{1}{2}\nabla^2 \; + \; V_{KS}(\mathbf{r})\right] \; \psi_i(\mathbf{r}) \; = \; \epsilon_i \; \psi_i(\mathbf{r}), \tag{1.7}$$

where the KS potential is

$$V_{KS}(\mathbf{r}) \; = \; V_{ext}(\mathbf{r}) \; + \; \int \frac{n(\mathbf{r}')}{|\mathbf{r}-\mathbf{r}'|}d\mathbf{r}' \; + \; V_{xc}(\mathbf{r}); \quad V_{xc}(\mathbf{r}) \; = \; \frac{\delta E_{xc}[n]}{\delta n(\mathbf{r})}, \tag{1.8}$$

and

$$n(\mathbf{r}) \; = \; \sum_{i=1}^{N} f(\epsilon_i - \epsilon_F)|\psi_i(\mathbf{r})|^2, \tag{1.9}$$

with $f(x)$ the Fermi-Dirac distribution and ϵ_F the Fermi energy fixed by the condition

$$\int n(\mathbf{r})d\mathbf{r} = N. \tag{1.10}$$

These are the famous KS equations, they must be solved self-consistently because V_{KS} is a functional of the orbitals itself. To this end we may use the Conjugate Gradient algorithm (see Appendix A.1) or the Davidson algorithm [36]. The latter is an iterative technique which requires a direct diagonalization of $N_{nbnd} \times N_{nbnd}$ matrices, where N_{nbnd} is the number of states in the system. Usually the computational cost of this direct diagonalization is very small. However, when the algorithm is implemented on a parallel machine also the direct diagonalization should be performed in parallel. In Appendix A.2 we describe our implementation.

When self-consistency is achieved the electronic energy of the system is:

$$E = \sum_{i=1}^{N} f(\epsilon_i - \epsilon_F)\epsilon_i - \frac{1}{2}\int \frac{n(\mathbf{r})n(\mathbf{r}')}{|\mathbf{r}-\mathbf{r}'|}d\mathbf{r} + E_{xc}[n] - \int V_{xc}(\mathbf{r})n(\mathbf{r})d\mathbf{r} + E^{ion}, \tag{1.11}$$

where E^{ion} is the ionic electrostatic repulsion term. This would be the *exact* electronic GS energy of the system if we knew $E_{xc}[n]$. Unfortunately the exact form of the XC energy is not (yet) known.

1.1.1 Local Density Approximation

The most widely used approximation for the XC energy is the so called *Local Density Approximation*: the dependence on the density is of the form

$$E_{xc}^{LDA}[n] = \int n(\mathbf{r})\epsilon_{xc}(n(\mathbf{r}))d\mathbf{r}, \tag{1.12}$$

and $\epsilon_{xc}(n)$ is taken to be the exchange and correlation energy per particle of a uniform electron gas whose density is $n(\mathbf{r})$. This has been accurately calculated using Monte Carlo simulations [37] and parametrized in order to be displayed in an analytic form [38].

By construction this approximation yields exact results if the density of the system is uniform, and should not be very accurate for those systems whose density is highly dis-homogeneous, as for example for atoms and molecules. However, it turns out to work better then expected for a wide range of materials. In molecules, for example, the LDA usually overestimates the binding energies, but it yields in general good results for equilibrium distances and vibrational frequencies.

Within this approximation, the exchange and correlation part of the KS potential is

$$V_{xc}^{LDA}(\mathbf{r}) = \frac{\delta E_{xc}^{LDA}[n]}{\delta n(\mathbf{r})} = \epsilon_{xc}(n(\mathbf{r})) + n(\mathbf{r})\frac{\partial \epsilon_{xc}(n)}{\partial n}. \tag{1.13}$$

Note that $E_{xc}^{LDA}[n] \neq \int V_{xc}^{LDA}(\mathbf{r})n(\mathbf{r})d\mathbf{r}$.

1.2 Infinite (periodic) systems

Now we have a complete procedure to calculate the GS density and the GS energy of the system. Given the Hamiltonian of the system one has to find the eigenvalues and the eigenvectors of the KS Eq. 1.7. The number of eigenvectors needed is proportional to the number of atoms in the system. It is clear that only systems containing a finite number of atoms can be studied in practice. However, if the system is a periodic solid, then the KS potential 1.8 is a periodic function of the lattice,

$$V_{KS}(\mathbf{r}+\mathbf{R}) = V_{KS}(\mathbf{r}), \tag{1.14}$$

for each Bravais lattice vector $\mathbf{R}$. Thus, we can use the Bloch theorem to write the general form of the solution of Eq. 1.7,

$$\psi_i(\mathbf{r}) = \psi_{n\mathbf{k}}(\mathbf{r}) = e^{i\mathbf{k}\cdot\mathbf{r}}u_{n\mathbf{k}}(\mathbf{r}), \tag{1.15}$$

where $\mathbf{k}$ is a vector in the first Brillouin zone (BZ) of the reciprocal lattice, $u_{n\mathbf{k}}(\mathbf{r})$ is a function with the periodicity of the Bravais lattice,

$$u_{n\mathbf{k}}(\mathbf{r}+\mathbf{R}) = u_{n\mathbf{k}}(\mathbf{r}), \tag{1.16}$$

and n is a degeneracy index which accounts for the band number [39]. For an insulator or a semiconductor, the number of occupied bands is equal to one half the number of electrons in the unit cell of the crystal. Putting Eq. 1.15 in Eq. 1.7 we have

$$[(-i\nabla + \mathbf{k})^2 \; + \; V_H(\mathbf{r}) \; + \; V_{xc}(\mathbf{r}) \; + \; V_{ext}(\mathbf{r},\mathbf{k})] \; u_{n\mathbf{k}}(\mathbf{r}) \; = \; \epsilon_{n\mathbf{k}} \; u_{n\mathbf{k}}(\mathbf{r}). \tag{1.17}$$

The dependence on $\mathbf{k}$ of the external potential is due to its possible non-locality in the variable $\mathbf{r}$, therefore we write $V_{ext}(\mathbf{r},\mathbf{k}) = e^{-i\mathbf{k}\cdot\mathbf{r}} V_{ext}(\mathbf{r}) e^{i\mathbf{k}\cdot\mathbf{r}}$, (see for example Ref. [11] for a discussion on the implementation of DFT with non-local potentials). To calculate the electronic properties of the system, such as the total energy and the ionic forces, integrations in the whole BZ are needed. As a consequence one in principle needs an infinite number of solutions of Eq. 1.17, i.e. for each $\mathbf{k}$-point of the BZ a number of eigenstates which depends on the number of electrons in the unit cell. Of course, in practice only a finite number of solutions can be found. However, one can check the quality of the approximation by systematically increasing the number of $\mathbf{k}$-points. If these points are badly chosen, the convergence is very slow. The right way to produce the points had been firstly invented by Baldereschi [40] (who proposed a scheme to use only one point!), and then improved by Chadi & Cohen [41] and Monkhorst & Pack (MP) [42]. If the quantity to be integrated is smooth, then a small number of special $\mathbf{k}$-points is needed. In the case of metals some additional care is needed. The integrals now have not to be done in the whole BZ anymore, but only inside the Fermi surface. This is the same thing of doing integrals in the whole BZ *cutting* the integrands at the Fermi surface and keeping them zero outside. This fact results in a discontinuity of the function to be integrated, which therefore is not smooth at all. For this reason a larger number of $\mathbf{k}$ -points is usually needed for metals. To speed up the convergence with respect the $\mathbf{k}$ -points sampling, a trick has invented by Fu & Ho [43]: one artificially smoothens the functions near the Fermi energy and substitutes the *cut* across the Fermi surface with an appropriate Fermi-Dirac like behaviour. This fact corresponds to the introduction of a fictitious electronic temperature which introduces an error in the integrals that depends on the electronic temperature and on the smearing function used [44]; however, it can be easily controlled.

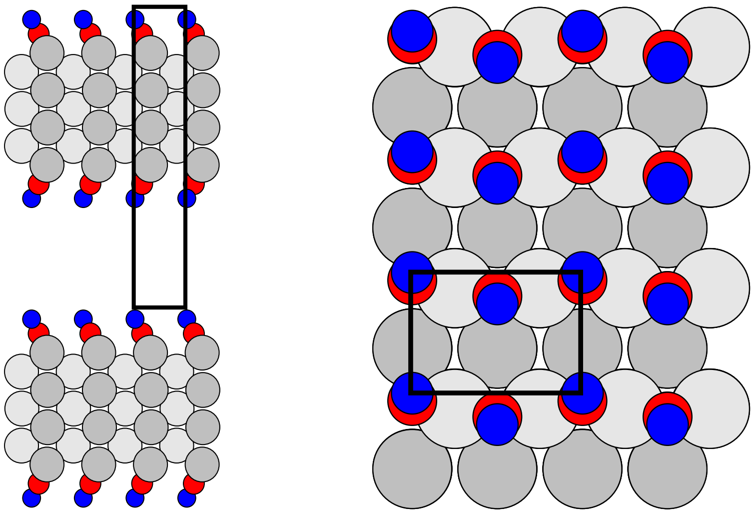

Figure 1.1: (Color) Unit cell (solid line) for the 1×1 Rh(110) surface covered by a complete layer of CO molecules in the 2×1 geometry.

1.3 Surfaces

A surface is a solid with no periodicity in the direction of its normal, say the z-axis. In this case all the formalism which has been described in the previous section is no more valid. However, it is easy to recast the surface problem in such a way that the three-dimensional periodicity is restored. In fact one can always construct a crystal unit cell as shown in Fig. 1.1, i.e. a slab formed by a certain number of atomic layers, plus a vacuum region. To describe the surface accurately the number of layers in the slab must be large enough so that the central layers resemble the bulk properties, and the vacuum region must be so thick that opposite surfaces do not interact with each other. In other words, the slab and the vacuum thickness must be larger than the surface states extension.

1.4 Plane-Wave Pseudopotential Method

Eq. 1.7 can be solved expanding the one-particle orbitals, $u_{n\mathbf{k}}(\mathbf{r})$, in a complete set of known functions. The most natural set of basis functions to describe a periodic system is provided by plane-waves (PW's). This is a complete orthonormal set, easy to handle, and does not depend on the position of the atoms in the unit cell.

The expansion in PW's reads:

$$u_{n\mathbf{k}}(\mathbf{r}) = \sum_{\mathbf{G}} e^{i\mathbf{G}\cdot\mathbf{r}} c_{n\mathbf{k}}(\mathbf{G}), \tag{1.18}$$

where $\mathbf{G}$ is a reciprocal lattice vector. Putting this expansion in Eq. 1.17 we find

$$\sum_{\mathbf{G}'} [\ |\mathbf{k}+\mathbf{G}|^2 \delta_{\mathbf{G},\mathbf{G}'} + V_H(\mathbf{G}-\mathbf{G}') + V_{xc}(\mathbf{G}-\mathbf{G}') + \\ + V_{ext}(\mathbf{k}+\mathbf{G},\mathbf{k}+\mathbf{G}')\ ]\ c_{n\mathbf{k}}(\mathbf{G}') = \epsilon_{n\mathbf{k}}\ c_{n\mathbf{k}}(\mathbf{G}). \tag{1.19}$$

We see that using PW's the KS equation has a very simple form. The KS eigenvalues have no physical meaning, but it turns out that their collection in reciprocal space resembles very much the band structures of the solids.

The number of PW's used in Eq. 1.19 is determined by the condition

$$|\mathbf{k}+\mathbf{G}|^2 \leq E_{cut}. \tag{1.20}$$

Playing with E_{cut} one can systematically increase the accuracy of the expansion. Eq. 1.20 defines a sphere in reciprocal space whose radius is $E_{cut}^{\frac{1}{2}}/\Omega_{BZ}^{\frac{1}{3}}$. where Ω_{BZ} is the volume of the BZ. The number of PW's inside this sphere is then

$$N_{pw} \approx \frac{4\pi}{3\Omega_{BZ}} E_{cut}^{\frac{3}{2}}, \tag{1.21}$$

which, for a fixed cutoff energy and then a fixed accuracy in the description of the KS wave-functions, is linear in the volume of the unit cell. Given a fixed accuracy the number of PW's needed depends on the shape of the KS orbitals. This depends on the details of the electronic structure which must be described. In a simple LCAO (Linear Combination of Atomic Orbitals) scheme the $c_{n\mathbf{k}}(\mathbf{G})$'s are the Fourier components of the atomic orbitals. Due to the localization of the core electrons and to the rapid oscillations in the core region of the wave-functions which describe the valence electrons, the number of PW's needed, even for a simple calculation, is huge.

We need approximations to avoid this problem. The first one is to disregard the core electrons because they do not participate to the chemical properties of matter, at least until their binding energy is much higher than the energy involved in the chemical properties one wants to study. So one "freezes" them around the nuclei and redefines the system as it was formed by "ions" plus "valence electrons". We are left with the second problem, how to deal with the oscillations in the core region of the valence wave-functions, due to the orthogonalization to the core wave-functions. The solution to this is the introduction of a *pseudopotential* (PP) which substitutes the ionic Coulomb potential in such a way that the valence *pseudo*-eigenvalues are the same as the all-electron (AE) ones and the *pseudo*-wave-functions coincide with the AE ones from a fixed core radius on, and are as smooth as possible below the core radius, with the only constraint to be normalized (*norm-conserving* (NC) pseudopotentials). To satisfy this requirements the PP usually must be angular momentum dependent, i.e pseudo-wave-functions corresponding to different angular momenta are eigenfunctions of different potentials. However, the long range behaviour of these different potentials must resemble the true one, because above the core radius the pseudo-wave-functions are identical to the AE ones. This mean that the difference must be confined in the core region and then the PP can be written in the following form: [45, 46, 47]

$$V_s^{sl}(\mathbf{r},\mathbf{r}') \;=\; V_s^{loc}(r)\delta(\mathbf{r}-\mathbf{r}') \;+\; \sum_{l=0}^{l_{max}} V_{s,l}^{nl}(r)P_l(\hat{\mathbf{r}},\hat{\mathbf{r}}')\delta(r-r'), \tag{1.22}$$

where $V_s^{loc}(r)$ is a local, long range part and approaches the AE potential above a cutoff radius r_c^{loc}, and $V_{s,l}^{nl}(r)$ are the non-local short range angular momentum dependent part, the index s refers to the atom, the superscript sl emphasizes the *semi-locality* (non local in angular momentum but local in r) and P_l is the projector onto the angular momentum l,

$$P_l(\hat{\mathbf{r}},\hat{\mathbf{r}}') \;=\; \sum_{m=-l}^{l} Y_{l,m}(\theta,\phi)Y_{l,m}^*(\theta',\phi'), \tag{1.23}$$

whit the $Y_{l,m}$'s the spherical harmonics. The quality of the PP depends on its transferability properties, i.e. the cability to reproduce the AE results over a wide range of electronic configurations.

1.4.1 Separable (Kleinman & Bylander) pseudopotentials

The computational cost for the application of the KS Hamiltonian in reciprocal space is proportional to N_{pw}^2 for each state. A particularly convenient form for the ionic PP has been introduced by Kleinman & Bylander [48]. If the PP is expressed in this form, the computational cost for each $H_{KS}|\psi\rangle$ operation scales as $N_{pw} \times N_{at}$ ($N_{at} << N_{pw}$). The construction of the PP is done in the following way. Consider the Schrödinger equation for the atom, let ψ_i be an eigenvector, $i = \{\epsilon_i lm\}$ is an index for the three atomic quantum numbers, we have

$$(T \ + \ V^{AE} \ - \ \epsilon_i) \ |\psi_i\rangle \ = \ 0. \tag{1.24}$$

Now we chose a cutoff radius r_{loc}^c and generate a smooth local potential V^{loc} in such a way that it is equal to the AE potential V^{AE} at an above r_{loc}^c (usually, V^{loc} is one of the l angular momentum conponents of the PP). The next step is the construction of a pseudo-wave-function ϕ_i in such a way that it matches the AE one at and above a different cutoff radius r_l^c, dependent on the l angular momentum, and that it has the same norm of the AE one: $\langle\phi_i|\phi_i\rangle_R = \langle\psi_i|\psi_i\rangle_R$, where $R = \max\{r_{loc}^c, r_l^c\}$, for all the angular momenta which are included, and the notation $\langle \ | \ \rangle_R = \int_0^R$ is meant. Now we define the local wave-function

$$|\chi_i\rangle \ = \ (\epsilon_i \ - \ T \ - \ V^{loc}) \ |\phi_i\rangle, \tag{1.25}$$

which vanishes at and above R, where $V^{loc} = V^{AE}$ and $\phi_i = \psi_i$, and we construct a "truly non-local" part for the PP in the following way:

$$V_l^{tnl} \ = \ \frac{|\chi_i\rangle\langle\chi_i|}{\langle\chi_i|\phi_i\rangle}, \tag{1.26}$$

so that the PP is non-local *both* in the angular momentum component *and* in the radial coordinate r:

$$V^{nl}(\mathbf{r}, \mathbf{r}') \ = \ V^{loc}(r)\delta(\mathbf{r} - \mathbf{r}') \ + \ \sum_{l=0}^{l_{max}} V_l^{tnl}(r, r')P_l(\hat{\mathbf{r}}, \hat{\mathbf{r}}'). \tag{1.27}$$

This form for the PP's must be used with some care. Due to the non-locality in the r variable, it is no more guaranteed that the eigenvectors of the atomic Hamiltonian can be ordered in term of increasing number of their nodes. This fact sometimes leads the appearance to unphysical states (*ghosts*), whose energy levels are near or even below those of the true states [49]. This problem can be usually solved with a suitable choice of the local part of the PP.

1.4.2 Ultra-Soft (Vanderbilt) pseudopotentials

The requirement of norm conservation for the pseudo-wave-functions can be a limiting factor for numerical calculations when also the valence electrons are very localized around their nuclei. This is a particular serious problem for first row elements, like carbon and more so for nitrogen, oxygen, and for transition metals, where the d-electrons are as localized as shallow core states but have an extraction energy which is comparable to valence energies, and for this reason cannot be excluded from the calculation. If this is the case the utilization of NC pseudopotentials requires huge PW's basis sets to achieve an acceptable accuracy. In a work published in 1990 Vanderbilt [50] showed that, introducing a generalized formalism, the norm conservation constraint can be removed. In this way one can construct much smoother pseudo-wave-functions, with the only constraint of matching the AE ones at and above a fixed core radius (see Fig. 1.2). The price to pay for having so smooth pseudo-wave-functions is the introduction of a new generalized formalism. Due to the fact that the pseudo-wave-functions are no more normalized, the charge density has to be restored by adding an "augmentation" part.

$$n(\mathbf{r}) \; = \; \sum_{n,\mathbf{k}} |\phi_{n\mathbf{k}}(\mathbf{r})|^2 \; + \; n_{aug}(\mathbf{r}), \tag{1.28}$$

and the KS equation has the new generalized form:

$$H_{KS}|\phi_i\rangle \; = \; \epsilon_i S|\phi_i\rangle, \tag{1.29}$$

where S is a non-local overlap operator.

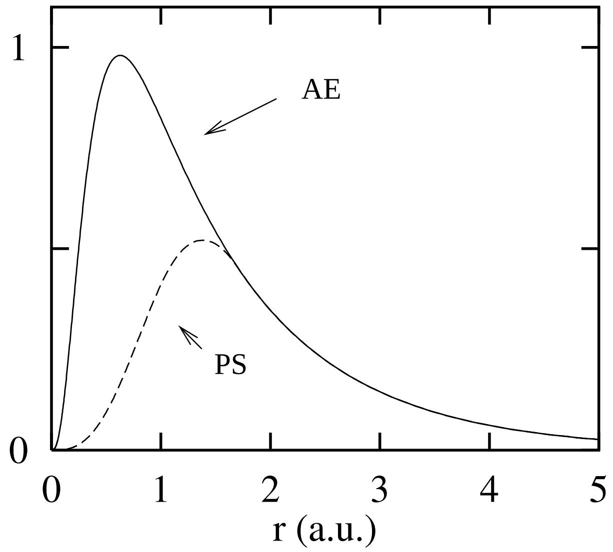

Figure 1.2: All-electron (solid) and Ultra-Soft pseudo (dashed) radial wave-functions of the $3d$ orbital of nickel. $r_c = 1.75$ a.u.

1.5 Forces

The knowledge of the forces among the atoms is a fundamental ingredient whenever one is interested in optimizing geometric structures, or studying the dynamical evolution of the system.

Ionic forces are the energy derivative with respect to the ions displacements. Using the Hellmann-Feynmann theorem [51], it is possible to obtain the forces without energy calculations for other ionic configurations that the actual one. This is a general result which applies for the energy derivative with respect to an arbitrary parameter λ, from which the external potential depends. In the case of forces, λ is the collection of the ionic positions. The energy derivative with respect to λ can be written as

$$\frac{\partial E}{\partial \lambda} = \int n_\lambda \frac{\partial V}{\partial \lambda}, \tag{1.30}$$

which only requires the knowledge of the "actual" density. Therefore, with only one self-consistent calculation, one has the total energy and the forces on the atoms.

Chapter 2

Results

In this chapter we present our results for carbon-monoxide adsorption on the (110) of rhodium and for oxygen adsorption on its (001) surface.

In the first case, we have studied the structure and the phase stability of one mono-layer (ML) of carbon-monoxide adsorbates on Rh(110). We have determined the most stable surface configuration and we have studied the finite temperature properties of the system, finding a critical temperature where an order-disorder transition occurs for the CO over-layer, agreement with the experimental findings [15].

In the second case, we have studied the oxygen adsorption on the Rh(001) surface and the peculiar 'clock' reconstruction it induces on the substrate [28]. The experimental data are not complete enough to determine uniquely the geometry of the reconstruction, and, in analogy with two similar systems, C/Ni(001) and N/Ni(001), where additional experimental data allow a more precise characterization of the reconstruction [29, 30, 31, 32], the same kind of behaviour of Rh(001) upon oxygen adsorption has been proposed. We show that this is not the case. Finally we present some preliminary results we have obtained on the related systems C/Ni(001), N/Ni(001), and O/Ni(001). In particular, we have found a 'clock' reconstruction for the C/Ni(001) and the N/Ni(001) systems which is in agreement with the experiments but it is different from the one we have found for O/Rh(001).

As a preliminary study we have determined the structural and electronic properties of rhodium bulk, as well as those of the isolated oxygen molecule, O_2, and carbon-monoxide, CO. We have found very good agreement with experimental data, this fact indicates the quality of our approximations (the LDA and the PP approximation).

2.1 Rhodium bulk

Rhodium has the face-centered cubic crystal structure. In order to determine the equilibrium lattice constant a_0 and the bulk modulus B_0, we have fitted to the Murnaghan's equation of state the calculated energies as a function of the unit cell volume:

$$E(V) = \frac{V_0 B_0}{B_0'} \left[\frac{1}{B_0' - 1} \left(\frac{V_0}{V} \right)^{B_0' - 1} + \frac{V}{V_0} \right] + const, \tag{2.1}$$

where B_0' is the derivative of B_0 with respect to the pressure and $V_0 = a_0^3/4$ is the equilibrium volume.

We have used the same *Ultra-soft* psudopotential of Ref. [52]. This PP has been constructed by relaxing the norm conservation constraint only for the d channel, while the s and p channels are constructed in the usual norm-conserving scheme. The core radii are respectively 1.6, 2.53 and 2.53 a.u. for the $4d$, $5s$ and $5p$ states. The $l = 1$ component of the PP has been assumed as the local part of the PP. With this prescription the isolated pseudo-atom is *ghost* free. We have used PW's up to a maximum kinetic energy of 30 Ry; BZ integrations have been done using 10 MP **k**-points in the IBZ and a smearing function of order 1 with a width of $\sigma = 0.03$ Ry, as in Ref. [53].

The resulting lattice constant is $a_0 = 3.81$ Å and the bulk modulus is $B_0 = 3.17$ Mbar, to be compared with the experimental values, $a_0 = 3.803$ Å and $B_0 = 2.69$ Mbar [54]. The comparatively poor agreement between the calculated and the experimental bulk modulus is not due to the PP approximation, as it is also in all-electron calculations. In Fig. 2.1, we display the total density of states (DOS) and its projection onto the atomic wave-functions (PDOS). [1]

The DOS is practically indistinguishable from the sum of the atomic PDOS's, thus indicating that the basis of the atomic wave-functions is almost complete for the solid.

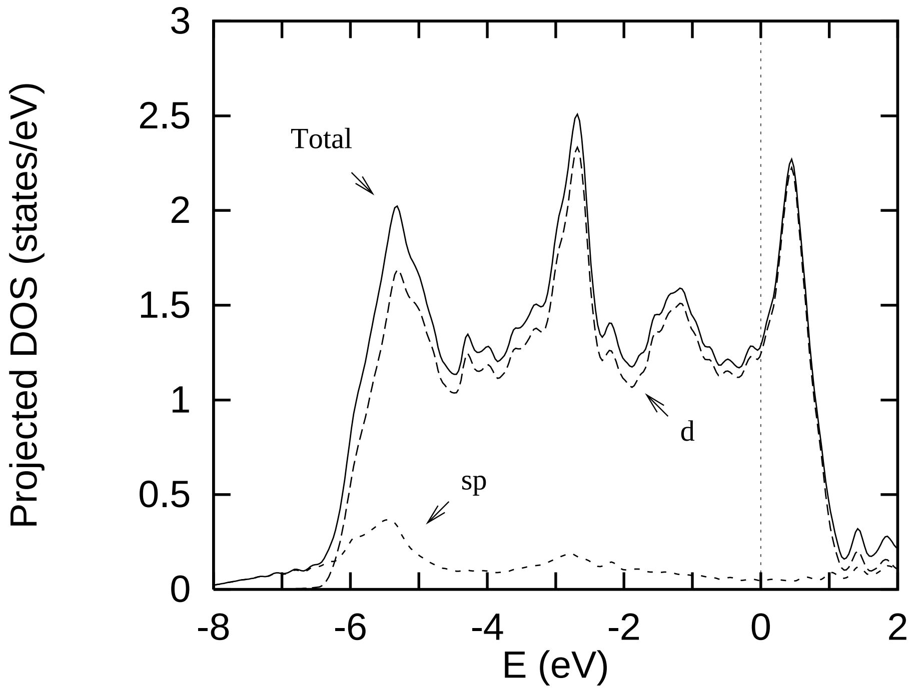

Figure 2.1: Total density of states and its projections onto the atomic wave-functions.

2.2 Molecular oxygen and carbon-monoxide

The oxygen PP is the same as in Ref. [55], with the $l = 2$ component taken as local reference, and cutoff radii respectively 1.0, 1.3 and 1.3 a.u. for the local potential and the $2s$ and $2p$ states respectively. The carbon PP has locality $l = 2$ and cutoff

[1]The projected DOS onto the atomic wave-function ϕ_s^{at} is:

$$n_s(E) \; = \; \int_{BZ} d\mathbf{k} |\langle \psi_{\mathbf{k}} | \phi_s^{at} \rangle|^2 \delta(E(\mathbf{k}) - E) \qquad (2.2)$$

where $\psi_{\mathbf{k}}$ is the solid wave-function at wave-vector $\mathbf{k}$.

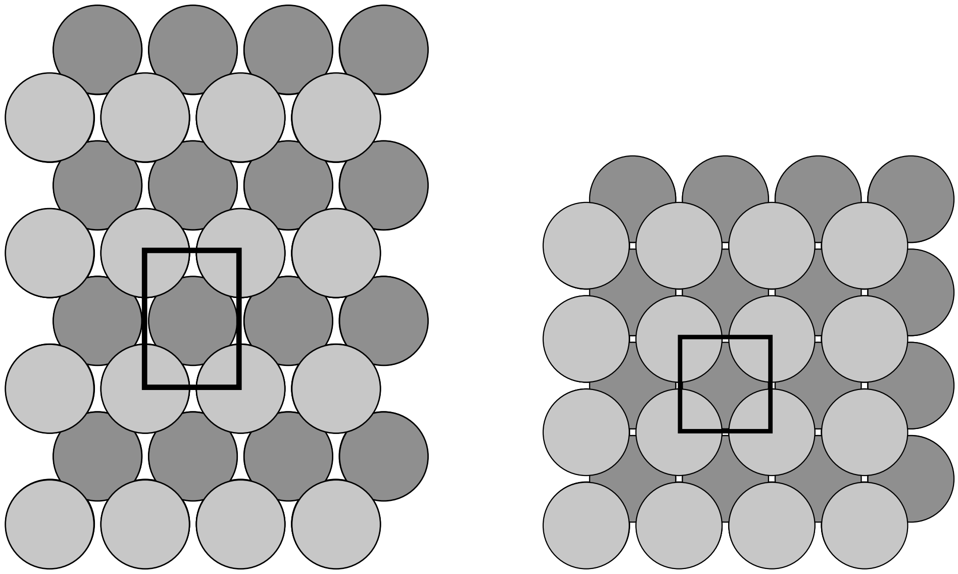

(a) Rh(110) (b) Rh(001)

Figure 2.2: Top view of the two rhodium surfaces investigated, the 1×1 unit cell is emphasized.

radii respectively 1.0, 1.1 and 1.1 a.u. for the local potential and the $2s$ and $2p$ states.

For the O_2 molecule we have found converged values for the equilibrium distance $R_0 = 1.22$ Å and for the vibrational frequency $\nu_0 = 1650$ cm^{-1} using the same cutoff energy we used for rhodium bulk. The corresponding experimental values are $R_0 = 1.21$ Å and $\nu_0 = 1580$ cm^{-1}.

The equilibrium distance of the CO molecule is $R_0 = 1.13$ Å and the vibrational frequency is $\nu_0 = 2075$ cm^{-1}. To be compared with the experimental values $R_0 = 1.13$ Å and $\nu_0 = 2170$ cm^{-1} [3].

2.3 Clean Rh(110) and Rh(001) surfaces

The isolated surfaces are modeled by periodically repeated super-cells (see Fig. 1.1 and Fig. 2.2). We have used the same super-cells for both the clean and the CO/O-covered surfaces [56]. For the clean (110) surface we have used 7 atomic layers plus a vacuum region corresponding to $\approx$ 9 layers ($\approx$ 12.5 Å). For the Rh(001) clean surface we have used 5 atomic layers plus a vacuum region corresponding to $\approx$ 6 layers ($\approx$ 11 Å). We have used the same Gaussian-smearing function as in the bulk calculations with $(8,4,2)$ and $(12,12,2)$ MP meshes for the (110) and the (001) surfaces respectively, resulting in 8 and 21 special $\mathbf{k}$-points in the 1×1 surface IBZ. Convergence tests performed with a value of σ twice as small and a correspondingly finer mesh of special points, has been resulted in no significant changes in total energies and equilibrium geometries. The latter are found by allowing all the atoms in the slab to relax until the force acting on each of them is smaller than 0.5×10^{-3}Ry/a_0.

The stable structure of the Rh(110) clean surface is unreconstructed. However, if prepared in a convenient way with oxygen adsorption, it may also present—upon thermal desorption—meta-stable $(1 \times n)$, $(n = 2,3,4,5)$, missing- or added-row structures which revert to the unreconstructed one at temperatures above 480 °K [6, 7, 8]. An analysis of LEED data suggests that the top interlayer spacing is reduced by $6.9 \pm 1.0\%$ relative to the bulk interlayer spacing, while the second interlayer spacing would expand by $1.9 \pm 1.0\%$ [57]. Our *ab-initio* data indicate a relaxation of -9% and of $+3.5\%$ in the first and second interlayer spacings respectively, in good agreement with experiments. Our calculated values for the surface energy, σ, and work function, ϕ, are reported in Table 2.1. A special care must be payed when estimating the latter. The XC potential goes to zero in the vacuum region much slower than the Hartree potential. The dependence of the former on the charge density is of the type $V_{xc} \propto n(\mathbf{r})^{1/3}$, while the latter has a dependence of the type $V_H \propto n(\mathbf{r})$. In the vacuum region the wave-functions go exponentially to zero with the distance from the surface, the decay characteristic length is inversely proportional to the work-function. This results in a decay characteristic length for the XC potential which is three times larger than that of the Hartree potential. However, at infinite distance from the surface they are both zero, therefore it is

	d_{12}/d_0	d_{23}/d_0	ϕ	σ	d_{12}/d_0	d_{23}/d_0	ϕ	σ
unit	%	%	(eV)	(eV/at)	%	%	(eV)	(eV/at)
	Rh(110)				Rh(001)			
LDA	-9	$+3.5$	5.1	2.0	-3.8	0	5.5	1.36
Expt.	-7^a	$+2^a$	5.1^b		-1.2 ± 1.6^c	0^c	5.0^d	1.27^e

[a] From Ref. [57], [b] From Ref. [58] [c] From Ref. [59], [d] From Ref. [60], [e] From Ref. [61].

Table 2.1: Structural data for the clean Rh(110) and Rh(001) surfaces. d_0 is the bulk lattice spacing, d_{12} the distance between the first and the second layer, d_{23} the distance between the second and the third layer, ϕ is the work function, and σ is the surface energy.

convenient to evaluate the vacuum level by simply neglecting the XC contributions (see Fig. 2.3).

For the Rh(001) surface we find that—in agreement with other *ab-initio* calculations [62, 63, 64]—the first layer relaxes inward by 3.8%, while the second layer is practically unrelaxed. The value of the first-layer relaxation reported in the experimental literature is anomalously small (the first interlayer spacing is practically equal to its bulk value within error bars). Recently, Cho and Scheffler [64] pointed out that a proper account of the vibrational contribution to the surface free energy may result in a reduction of the inward relaxation of the first layer, thus bringing theoretical predictions in better agreement with experiments. No attempts of estimating these vibrational effects have been done in the present work.

2.4 The structure and phase stability of CO on Rh(110)

The study of the carbon-monoxide adsorption on the transition metal surfaces is of fundamental importance in order to understand the physics of the reaction $2CO + 2NO \rightarrow 2CO_2 + N_2$. CO does not dissociate upon adsorption on the surface, while NO dissociates. The first product of the right hand side of the reaction is

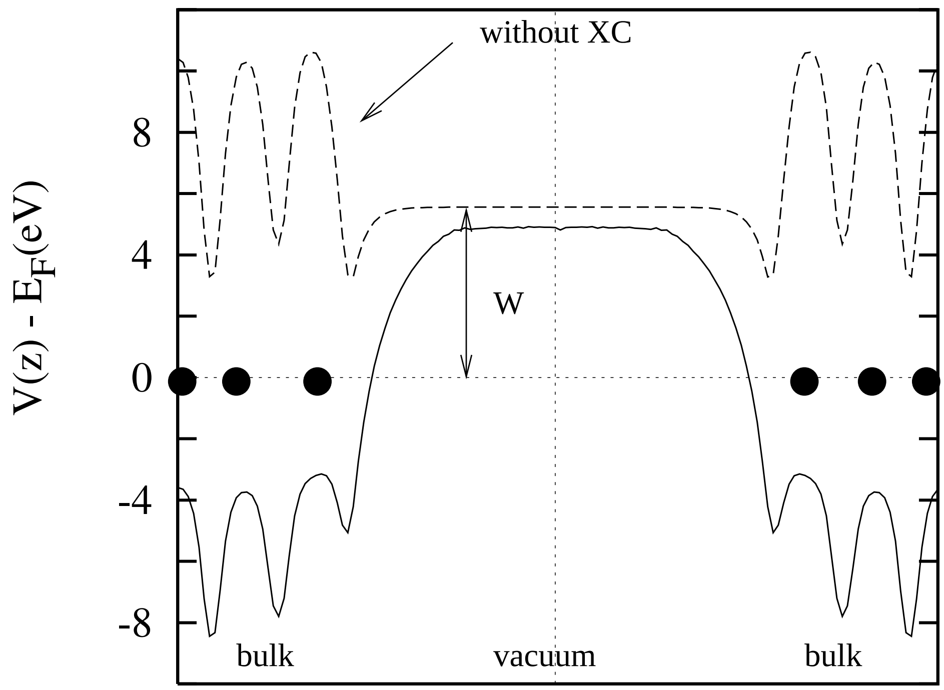

Figure 2.3: Planar average of the total potential energy (full line) and total potential energy without XC (dotted line) as function of the one dimensional coordinate orthogonal to the surface. The potential energy without XC converges more rapidly to the vacuum level with respect to the slab vacuum thickness.

realized when the adsorbed CO's recombine with the adsorbed oxygen atoms which come from the NO dissociations. It is therefore important to know which are the CO adsorption sites, how CO binds to the surface and how its interaction with the adsorbed O atoms is (possibly) mediated by the surface.

The work contained here is aimed at the identification of the ground-state configuration of one ML of CO molecules adsorbed onto the Rh(110) surface. Moreover, we have studied the finite temperature properties of this system and we have found that there is an order-disorder transition for the CO over-layer. Our findings are in good agreement with experimental data [15, 18].

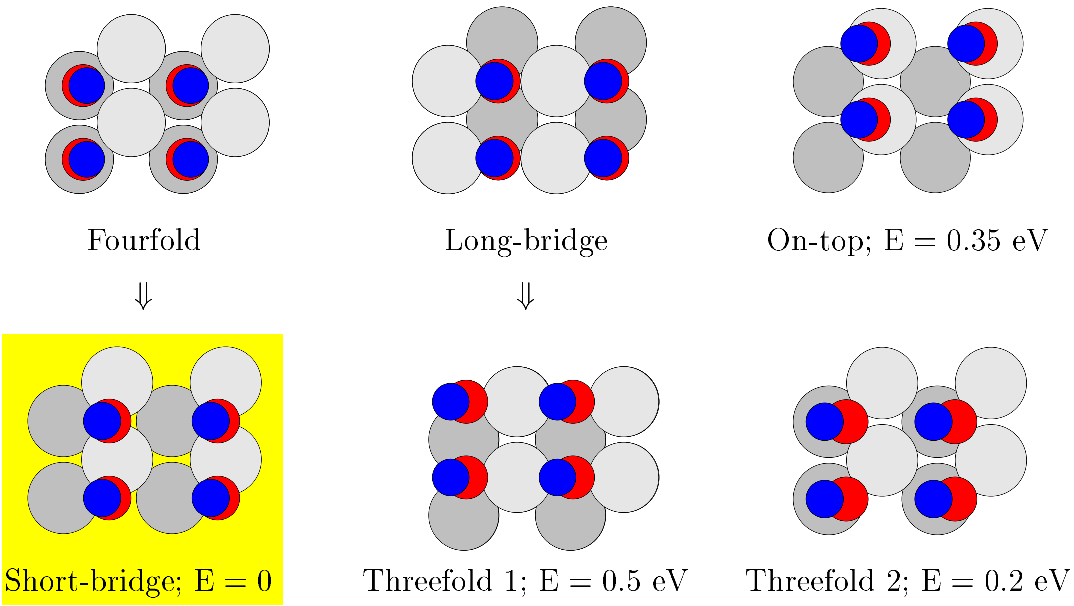

Figure 2.4: (Color) The six different explored adsorption sites.

2.4.1 Structural analysis

For the CO-Rh(110) system, LEED I-V data indicate that the molecules are bound in the *short bridge* site between two first layer rhodium atoms in the $(1\bar{1}0)$ direction with the molecular axis tilted by 24 ± 4 degrees from the surface normal, forming a (2×1)p2mg structure [18]. In principles there are many different ways to arrange the CO molecules so as to obtain the same LEED pattern. However, a careful analysis of the LEED intensity allows one to assign which is the most probable adsorption site among those compatible with the surface ordering. From this point of view this experimental technique give essentially the same informations one is able to find out from an *ab-initio* calculation where, using the energetics, it is possible to compare different atomic configurations which correspond to different local minima (or saddle-points) for the total energy. The absolute minimum is somewhere, but it is not always directly accessible. We concentrate our attention on six possible adsorption sites (see Fig. 2.4):

- *Fourfold* site, in the center of a rectangle formed by four first-layer atoms;

unit	d_{12}/d_0 %	α degrees	δ degrees	$d(\mathrm{C-O})$ Å	$d(\mathrm{Rh-C})$ Å	ΔE meV/mol
Expt.[a]	$+3 \pm 2$[b]	24 ± 4	13 ± 4	1.13 ± 0.09	1.97 ± 0.09	
2×1	+2.8	17 ± 2	13 ± 2	1.17	2.02	0.0
1×1	+2.8	≤ 10	≤ 10	1.17	2.02	33.5
1×2	+2.8	≤ 5	≤ 5	1.17	2.02	33.5
2×2	+2.4	13 ± 2	11 ± 2	1.17	2.02	13.5
$2 \times 2'$	+2.4	13 ± 2	11 ± 2	1.17	2.02	21.5
4×1	+3.7	16 ± 2	13 ± 2	1.17	2.02	17.0
$4 \times 1'$	+3.6	16 ± 2	12 ± 2	1.17	2.02	17.0

[a] From Ref. [18], [b] From Ref. [65]

Table 2.2: Structural data for seven different surface structures (see Fig. 2.5). d_{12} is the distance between the first and the second rhodium layers, d_0 the bulk interlayer distance, α and δ are respectively the angles between the surface normal with the C-O and the Rh-C axis, $d(\mathrm{C-O})$ and $d(\mathrm{Rh-C})$ are the C–O and the Rh–C distances ΔE is the energy difference per molecule between the $(n \times m)$ and the (2×1) structures. The theoretical error is estimated to be ≈ 2 meV. The experimental values refer to the (2×1) structure.

- *Long bridge* site, formed by two first-layer atoms in the (001) direction;
- *On-top* site, in which the CO molecule is located on top the first-layer atoms;
- *Short-bridge* site, formed by two first-layer atoms in the $(1\bar{1}0)$ direction ;
- *First threefold* site, formed by two first-layer atoms in the $(1\bar{1}0)$ direction and one second-layer atom;
- *Second threefold* site, formed by two second-layer atoms in the $(1\bar{1}0)$ direction and one first-layer atom.

The *Fourfold* and the *Long-bridge* sites are saddle-points. The nearest local minima are, respectively, the *Short-bridge* and the *First threefold* sites.

In agreement with the outcome of the LEED analysis, we find that the *Short-bridge* site is the most stable. The relative energies of the other three sites with respect to the *Short bridge*—assuming a (1×1) structure in all cases—are: 0.5 eV (*First threefold*), 0.2 eV (*Second threefold*) and 0.35 eV (*On top*). We find that the angle between the surface normal and the CO molecular axis is $\alpha = 17 \pm 2$ degrees, and that the angle between the Rh-C bond and the surface normal is $\delta = 13 \pm 2$ degrees; the Rh-C bond length is 2.02 Å and the C-O distance is 1.17 Å. The rhodium substrate presents an outward relaxation of the first layer of 2.8% with respect to the bulk interlayer spacing. These results are summarized in Table 2.2 together with similar ones obtained for six other different surface geometries (See Fig. 2.5).

From Table 2.2 we see that the (1×1) and (1×2) geometries are degenerate within our error bar which we estimate to be ±1 meV/molecule, and that the uncertainty on the corresponding tilt angle is very large. This behavior can be understood by a simple qualitative model of the surface energetics which also accounts for the observed ordering of the structures. In order to disentangle the relative importance of the adsorbate-substrate and adsorbate-adsorbate interactions, we have modeled the former by a (2×2) super-cell in which a single CO molecule is constrained to sit at the same short-bridge site which would be preferred at full coverage. We observe that the dependence of the adsorption energy on α is very weak up to $\alpha \approx 10^{\circ}$, and that it becomes very steep above this angle. The same behaviour is also observed for the δ angle. When the coverage increases, the dipole-dipole interaction becomes important and accounts qualitatively for the energy ordering of the structures displayed in Fig. 2.5. In the (2×1) structure, nearest-neighbor molecules are tilted by opposite angles around the axis joining them (the $(1\bar{1}0)$ direction), while next-nearest-neighbor molecules are tilted by a same angle about the (001) axis which joins them. The dipole-dipole interaction favors both these arrangements of angles. The (2×2) geometry is similar to the previous one as regards the nearest-neighbor interactions, whereas it is unfavored regarding next-

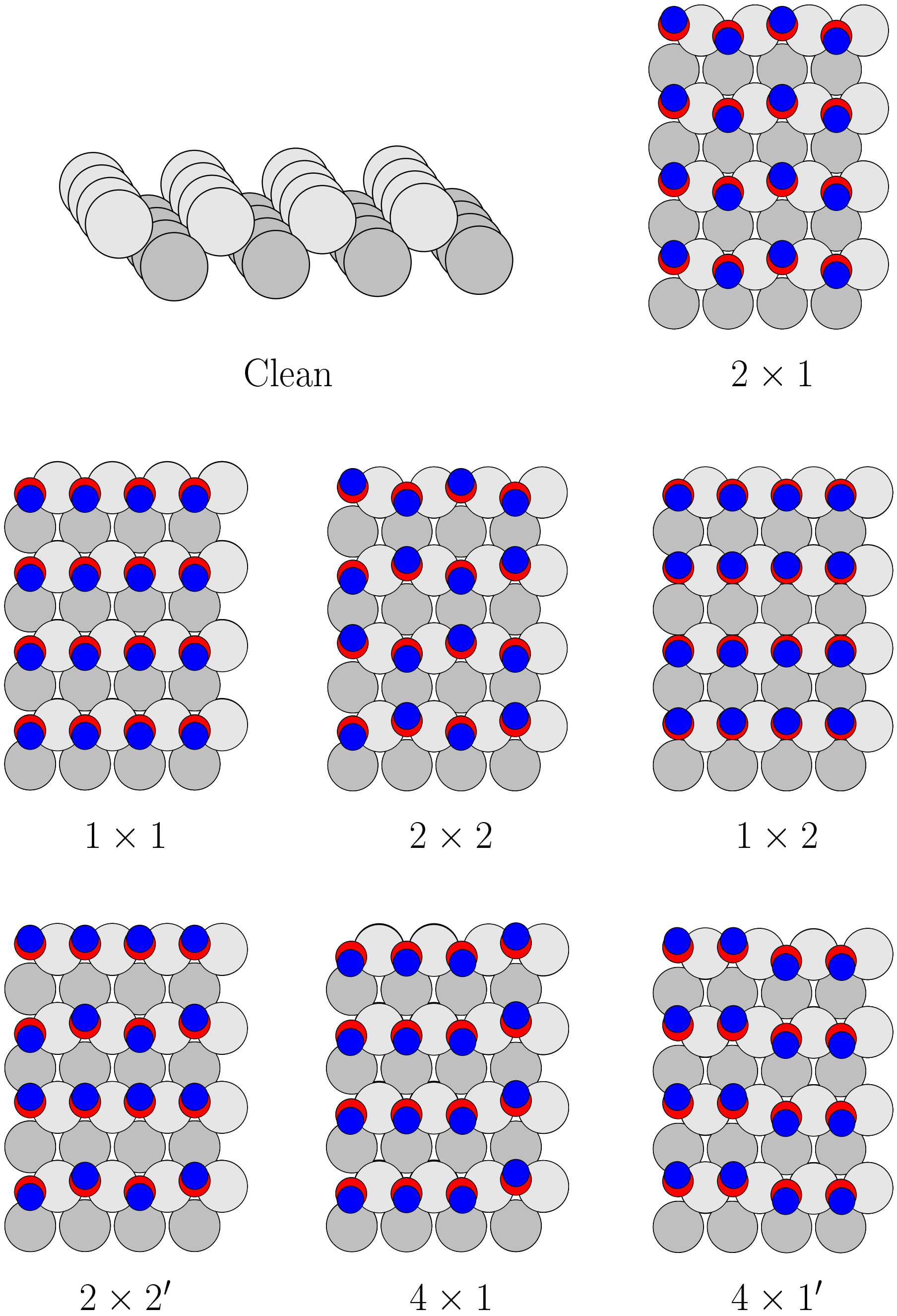

Figure 2.5: (Color) The seven different surface structures referred in the text and the clean Rh(110) surface.

nearest-neighbor interactions. The next higher energies are those of the (4×1) and $(4 \times 1')$ structures which are almost degenerate because they have the same number of unlike tilt angles along the $(1\bar{1}0)$ row. The next structure is the $(2 \times 2')$ one, which is characterized by an alternating arrangements of energetically favored and disfavored rows and columns of CO molecules. Finally, in the (1×1) and (1×2) structures, the nearest-neighbor molecules are tilted by a same angle and the corresponding dipolar interaction is therefore independent of α; it is only the weaker next-nearest-neighbor interaction which depends on α, more so for the (1×2) structure for which the sign of the dipole-dipole interaction energy is the same as that of the adsorbate-substrate interaction, while the two interactions tend to cancel for the other structure. In both cases, this behavior results in a very weak dependence of the energy upon α, and in an energy degeneracy of the two structures, within our error bars.

We have also calculated the adsorption energy of the CO molecules defined as

$$E_{ad} = E_{slab}^{\mathrm{Rh-CO}} - E_{slab}^{\mathrm{Rh}} - E_{slab}^{\mathrm{CO}}, \tag{2.3}$$

where $E_{slab}^{\mathrm{Rh-CO}}$ is the total energy of the CO covered surface, E_{slab}^{Rh} is the total energy of the clean Rh(110) surface, and $E_{slab}^{\mathrm{Rh-CO}}$ is the total energy of the CO, all the calculations being done using the same slab geometry and the same set of $\mathbf{k}$-points. The calculated adsorption energy is of 2.78 eV/molecule, which has to be compared to the experimental value 1.1 eV/molecule [13]. This large discrepancy is a common feature of the LDA, which is well known to overestimate absolute binding energies, whereas equilibrium geometries and energy differences among them are usually predicted with a much higher accuracy (of the order of a few percents).

2.4.2 Finite-temperature properties

To study the finite temperature properties of a system one should know its partition function $Q(\beta) = \sum_i e^{-\beta E_i}$, where $\beta = 1/K_B T$, K_B is the Boltzmann constant, T is the temperature, E_i is the energy of the i-th configuration and the sum extents over all the possible configurations. This is usually a prohibitively costly task, since the number of configurations, even for simple systems, is huge. However, we see from the form of the partition function that—at least in the low temperature limit—only the low-lying energy configurations give an appreciable contribution, being exponentially less and less important as their energy is higher and higher. Moreover, the partition function does not depend on the system from which it comes from. Taking advantage from this fact one can "map" the original system onto a much simpler one (a model), provided this new system has a similar partition function to the real one, at least for the temperature range one is interested in. Then, one is allowed to study the finite temperature properties of the model and to extend them to the real system.

From Table 2.2 we see that the energy necessary to tilt the angle of a molecule is of the order of $10 \div 30$ meV, whereas the energy difference between different adsorption sites is typically ten times as large. This fact indicates that—for temperatures up to a few hundreds °K—the relevant configurations which determine thermal equilibrium are all characterized by the molecules staying at their favorite adsorption sites (*short bridge*), while differing by their tilt-angle distributions only. Because of this we characterize each configuration by a set of tilt angles, $\{\vartheta_i, \varphi_i\}$, where ϑ_i, is the azimuthal angle of the i-th molecule with respect to the (110) direction, and φ_i is its polar angle with respect to $(1\bar{1}0)$ (see Fig. 2.6). We find that the energy differences among configurations can be accurately modeled by dipolar like molecule-molecule interactions up to third-nearest neighbors and by an interaction of each molecule with the substrate of the form:

$$B(\vartheta, \varphi) = \cos^2\varphi \left(a_2\vartheta^2 + a_4\vartheta^4\right) + \sin^2\varphi \left(b_2\vartheta^2 + b_4\vartheta^4\right). \tag{2.4}$$

The Hamiltonian of this *dipole model* is:

$$\begin{aligned} H \;=\; \frac{1}{2}\sum_{i,j}\Big(\sum_{\delta,\delta'=\pm1} & A_x(\mathbf{d}_{i,j}\cdot\mathbf{d}_{i+\delta,j} - 3(\mathbf{d}_{i,j}\cdot\mathbf{n}_{i+\delta,j})(\mathbf{d}_{i+\delta,j}\cdot\mathbf{n}_{i+\delta,j}) \;+ \\ &+\; A_y(\mathbf{d}_{i,j}\cdot\mathbf{d}_{i,j+\delta} - 3(\mathbf{d}_{i,j}\cdot\mathbf{n}_{i,j+\delta})(\mathbf{d}_{i,j+\delta}\cdot\mathbf{n}_{i,j+\delta})) \;+ \\ +\; A_2(\mathbf{d}_{i,j}\cdot\mathbf{d}_{i+\delta',j+\delta} - 3(\mathbf{d}_{i,j}\cdot\mathbf{n}_{i+\delta',j+\delta})&(\mathbf{d}_{i+\delta',j+\delta}\cdot\mathbf{n}_{i+\delta',j+\delta}) \;+\; B_{i,j}\;\Big), \end{aligned} \tag{2.5}$$

where the sum extents over all the surface sites, $\mathbf{d}_{i,j}$ is a normalized vector (versor) which defines the direction of the molecule in the site $\mathbf{R}_{i,j}$, $\mathbf{n}_{i+\delta',j+\delta} = \frac{\mathbf{R}_{i,j}-\mathbf{R}_{i+\delta',j+\delta}}{|\mathbf{R}_{i,j}-\mathbf{R}_{i+\delta',j+\delta}|}$

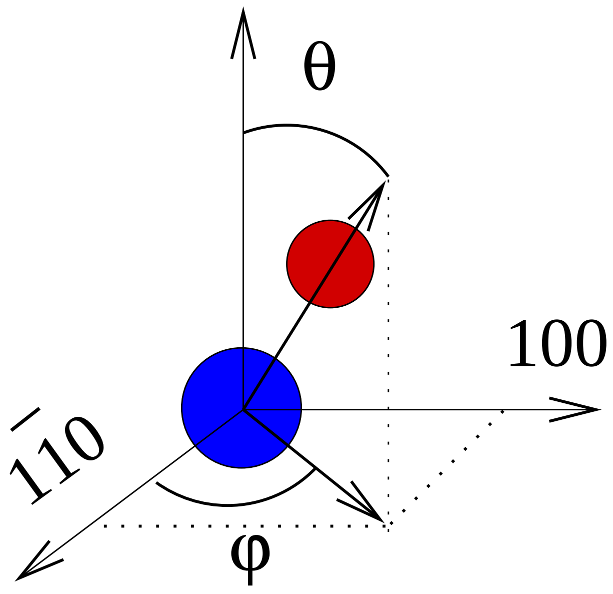

Figure 2.6: (Color) The CO molecule.

is the versor which connects the two surface lattice positions $\mathbf{R}_{i,j}$, and $\mathbf{R}_{i+\delta',j+\delta}$ and $B_{i,j} \equiv B(\vartheta_i, \varphi_j)$. Interactions up to third nearest neighbors are taken into account. The Hamiltonian is fully specified once we know the value of the seven parameters $\{a_2, a_4, b_2, b_4, A_x, A_y, A_2\}$. To determine these parameters the energies calculated for the structures in Fig. 2.5 are not enough. This can be easily realized noting that these structures do not contain any information about configurations with $\varphi \neq \pm\frac{\pi}{2}$. Thus, eight additional structures in the 1×1 configuration have been calculated, four of them for $\varphi = 0$ and different values of ϑ, which correspond to the molecule tilted along the $(1\bar{1}0)$ direction, the other four for $\varphi = \frac{\pi}{2}$, corresponding to configurations where the molecules are tilted along the (100) direction.

In order to calculate the energy landscape as a function of the tilt angle ϑ a constrained minimization is needed. One has to relax all the degrees of freedom but the tilt angle ϑ, which has a fixed value. In Appendix B it is explained how we have proceeded. Essentially, an extra term is added to the forces in order to keep zero the "force component" which would change ϑ.

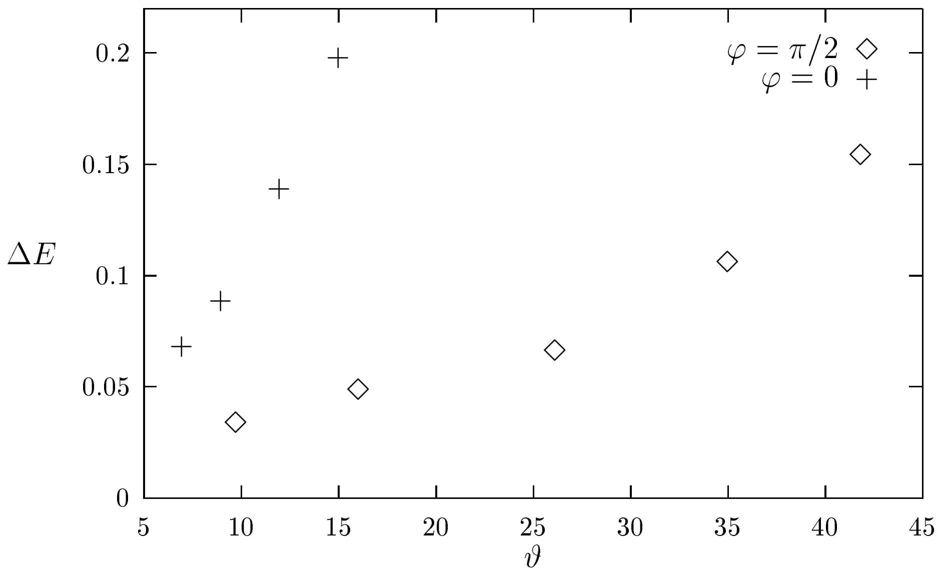

Figure 2.7: Energy difference (eV) from the 2×1 ground-state structure as a function of the tilt angle ϑ of the molecule in the (100) direction ($\varphi = \pi/2$) and in the $(1\bar{1}0)$ direction ($\varphi = 0$). Values calculated for the 1×1 geometry.

In Fig. 2.7 we report the calculated energies as a function of ϑ for two possible directions, $\varphi = 0$ and $\varphi = \pi/2$. The dependence on ϑ is much steeper in the $(1\bar{1}0)$ direction ($\varphi = 0$), denoting the "preference" of the molecules to be rather tilted along the (100) direction ($\varphi = \pi/2$). Fitting the dipole energy 2.5 with these eight values plus those of Table 2.2 we found the following best values for the parameters:

$$A_x = \quad 1.67 \text{ eV}; \quad A_y = -0.3 \text{ eV}; \quad A_2 = -0.64 \text{ eV};$$

and

$$\begin{aligned} a_2 &= -1.75 \text{ eV/rad}^2; \quad a_4 = \quad 3.7 \text{ eV/rad}^4; \\ b_2 &= \quad 35.8 \text{ eV/rad}^2; \quad b_4 = \quad 16.2 \text{ eV/rad}^4. \end{aligned}$$

Using this values we have a mean square error between fitted and calculated energies of 1.5 meV/molecule, with a maximum error of 3 meV. The error in the equilibrium value of the ϑ angle is of the order of a few degrees. Now, noting that the b's are one order of magnitude larger then the a's, we make a further approximation and assume that all the molecules are frozen in the positions corresponding to $\varphi = \pm\frac{\pi}{2}$.

Mapping onto a 2D Ising model

These two values of the φ angle can be conveniently labelled by an Ising variable, $\sigma = \mathrm{sign}(\varphi)$. Much in the same spirit of the *cluster expansion* of the energy landscape of an alloy [66], the energy of each tilt-angle configuration can be expressed in terms of polynomials in the σ's. [2] Because of symmetry, odd-power polynomials are absent from the cluster expansion. Restricting ourselves to second-order polynomials (spin-pair interactions) and neglecting all the couplings beyond next-nearest-neighbors, the cluster expansion of the surface energy reads:

$$E[\{\sigma\}] \;=\; \frac{1}{2}\sum_{i,j}\sigma_{i,j}\left(J_x\sum_{\delta=\pm1}\sigma_{i+\delta,j} \;+\; J_y\sum_{\delta=\pm1}\sigma_{i,j+\delta} \;+\; J_2\sum_{\delta,\delta'=\pm1}\sigma_{i+\delta,j+\delta'}\right). \quad (2.6)$$

It is straightforward to see that:

$$\begin{array}{rclrcl} E_{2\times1} &=& J_y - J_x - 2J_2; & E_{1\times1} &=& J_x + J_y + 2J_2; \\ E_{1\times2} &=& J_x - J_y - 2J_2; & E_{2\times2} &=& 2J_2 - J_y - \; J_x; \\ E_{4\times1} &=& E_{4\times1'} = J_y; & E_{2\times2'} &=& 0, \end{array} \quad (2.7)$$

where the subscripts refer to the structures of Fig. 2.5.

$E_{2\times1}$ is the ground-state energy which we take as the reference energy. The (4×1) and $(4\times1')$ structures are degenerate within the present model, and their energy difference provides therefore an estimate of the strength of longer-range or many-spin interactions which have been neglected. Out Eqs. 2.7, one can extract four independent energy differences, which are linear functions of the three parameters J_x, J_y, and J_2. By disregarding one of these equations in turn, one obtains 4 different linear systems for the J's which provide estimates for these parameters, which coincide within $\approx$ 1 meV. The average of the four set of parameters so obtained is:

$$J_x \;=\; 13.6 \text{ meV}, \quad J_y \;=\; -3.4 \text{ meV}, \quad J_2 \;=\; 1.7 \text{ meV}. \quad (2.8)$$

[2] We associate to each given distribution of Ising variables, $\{\sigma_i\}$, an energy defined as the minimum with respect to the ϑ's of the energy calculated at fixed φ's: $E[\{\sigma\}] \equiv \min_{\{\vartheta\}} E[\{\vartheta, \sigma\frac{\pi}{2}\}]$.

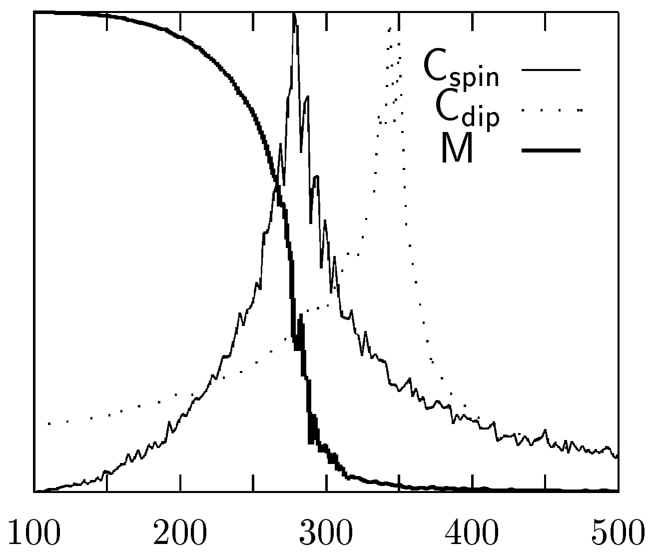

Figure 2.8: Fourier transform of the correlation function as a function of the temperature (°K) for the 2D spin model and specific heat for the spin and the dipole models (see text).

Note the large difference between the absolute values of J_x and J_y, which is due to a stronger coupling in the 'ziz-zag' $(\bar{1}10)$ direction, where the distance between neighboring molecules is smaller by a factor $\sqrt{2}$ than in the orthogonal direction.

Monte Carlo simulations

The thermal properties of our system are obtained by standard Metropolis Monte Carlo simulations of the above Ising model [67]. To this end, we have used a 32×32 square lattices with periodic boundary conditions. The simulations have been done starting at a high temperature ($T > 650$°K) and cooling down the system with small temperature steps (≈ 2°K). The order parameter of the transition between the (2×1) ordered phase and the disordered phase where the tilt angles are distributed at random, is the Fourier coefficient of the spin-spin correlation function, $M(\mathbf{q}) = \frac{1}{N} \sum_{\mathbf{r}} e^{i\mathbf{q}\cdot\mathbf{r}} \langle \sigma_{\mathbf{r}} \sigma_{\mathbf{0}} \rangle$, at wave-vector $\mathbf{q} = (\pi, 0)$, $\mathsf{M} = M(\pi, 0)$. The order-disorder transition temperature, T_c^{Is}, is estimated looking at the maximum of the specific heat C. We have not attempted any finite-size scaling, but we have verified that the location of the transition temperature is rather insensitive to the choice of the size of the system, by making a few simulations for a 64×64 system. In Fig. 2.8 we show the behavior of the specific heat, C, and the order parameter, M, as functions of temperature. Also shown in Fig. 2.8, it is a comparison between the specific heats as calculated from the simulations of the Ising model and from an independent simulation performed for the dipole model described in section 2.4.2. The Ising critical temperature is $T_c^{Is} = 280^{\circ}$K, while for the dipole model it is $T_c^{dip} = 340^{\circ}$K. The statistical error on these temperatures is of a few degrees only. Based on this figures and on a rough estimate of the dependence of the transition temperatures upon the value of the parameters of the two models, we conclude that an order-disorder $(2 \times 1) \rightarrow (1 \times 1)$ transition occurs at a critical temperature of $T_c \approx 300^{\circ}$K with an error bar smaller than 100°K.

After cooling down the system, when the temperature reached $\approx 50^{\circ}$K, well below the formation of the ordered structure, we heated up the system using the same temperature steps. For every size of the simulation lattice we observed no hysteresis. This fact is an indication of the second-order character of the transition. The experimental characterization of the order of the transition is not trivial, since it is necessary to heat the sample well above the critical temperature. However, the CO desorption temperature is near the order-disorder transition temperature, therefore it is not easy to heat up the system above T_c without losing some molecules. In this case, after freezing again the sample below the critical temperature, there is no guarantee that the system is the same as it was before the heating.

2.5 The reconstruction of Rh(001) upon O adsorption

As surfaces can modify the electronic properties of the atoms and/or the molecules which adsorb on them, in the same way the adsorbates can modify the structure and the chemical properties of the substrate they adsorb on. This is what happens, for

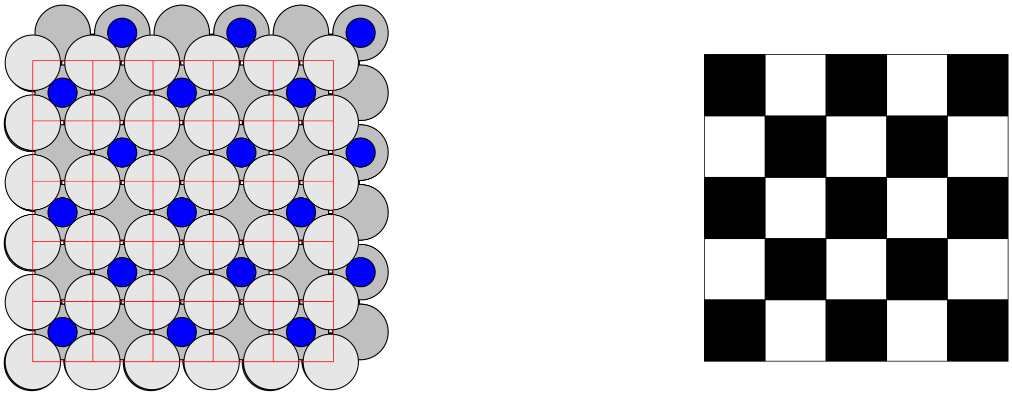

(a) c(2 × 2)

(b) chess-board

Figure 2.9: (Color) The c(2 × 2) structure (a) and its representation as a chess-board (b).

example, on the (001) surface of rhodium upon oxygen adsorption. In this case in fact the surface undergoes a reconstruction which is induced by a saturated oxygen over-layer [28]. A similar reconstruction is observed for the systems C/Ni(001) and N/Ni(001) [29, 30, 31, 32].

The adsorption of oxygen on Rh(001) is dissociative and the atoms fill the four-fold substrate sites in a c(2×2) geometry, the resulting saturation coverage is $\Theta = \frac{1}{2}$ ML. This geometry may be seen as a chess-board whose 'black' squares are occupied by oxygen atoms, while the 'white' ones are empty (see Fig. 2.9). Within this picture, the reconstruction observed in Ref. [28] can be described as a rotation of the 'black' or the 'white' squares, resulting in a (2×2)p4g symmetry.

There are two possible reconstructions of the substrate which are compatible with the experimental STM and LEED data [28]. the first one is a clockwise and counterclockwise rotation of the 'black' (filled) squares (Fig. 2.10a) and the second is a rotation of the 'white' (empty) squares (Fig. 2.10b). However, in analogy with the C/Ni(001) and the N/Ni(001) systems, where additional LEED I-V [32] and SEXAFS [33] data allow a more precise characterization of the reconstruction, in

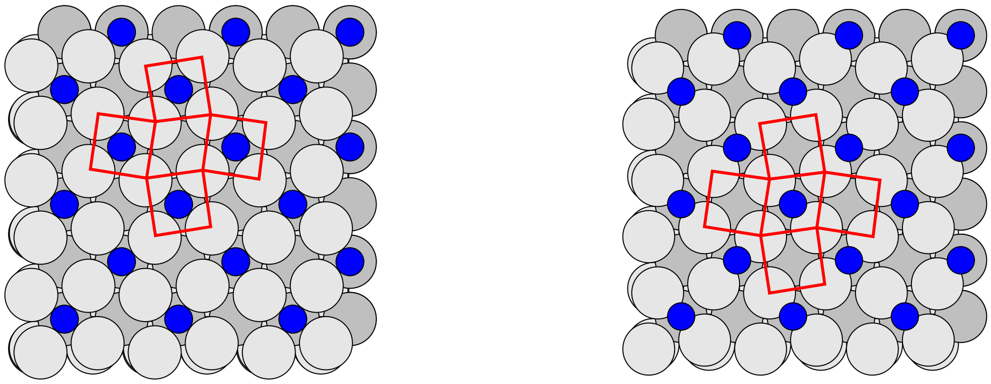

(a) 'Black' reconstruction

(b) 'White' reconstruction

Figure 2.10: (Color) The two possible reconstructions compatible with LEED and STM data of Ref. [28].

Ref. [28], a 'black' reconstruction is proposed also for the O/Rh(001) system.

As a preliminary study of oxygen adsorption, we have performed a couple of simple *ab-initio* molecular dynamics simulations of a O_2 molecule impinging onto the surface. The integration of the equation of motion has been done using the Verlet algorithm [68] with a time step of 50 a.u., corresponding to ≈ 1.2 femtoseconds (see Appendix C). We have tried two possible initial conditions for the molecule, in both of which the axis of the molecule is parallel to the surface. In the first case the projection of the center of the molecule on the surface falls on top of a surface atom, while in the other it falls on a bridge site (see Fig. 2.11). The initial velocity of the molecule is orthogonal to the surface and its modulus corresponds to a temperature of 300°K, while the surface is initially at zero temperature. The initial distance of the molecule from the surface is ≈ 6 atomic units and it is essentially in the vacuum. When the molecule arrives at the surface it breaks the molecular bond and then it dissociates. In Fig. 2.12 we display the Born-Oppenheimer (BO) potential energy, the total energy (i.e. the BO potential energy plus the ionic kinetic energy) and the O$-$O distance as functions of time. The total energy is essentially

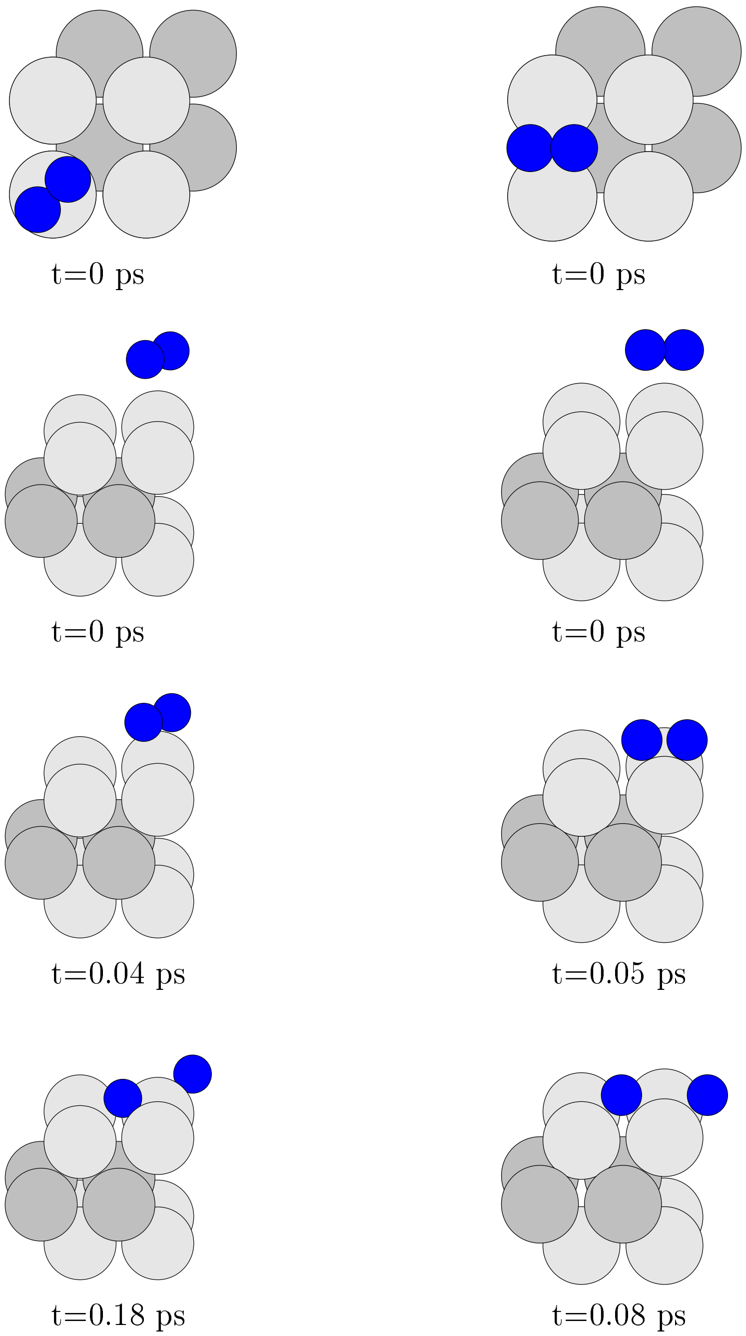

Figure 2.11: (Color) A few snapshots of two simple molecular dynamics simulations, corresponding to two different starting trajectories for the impinging molecule. In the last one it is evident the dissociation of the molecule.

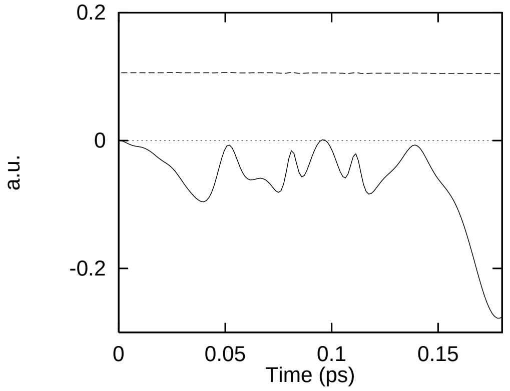

(a) On-top, energies

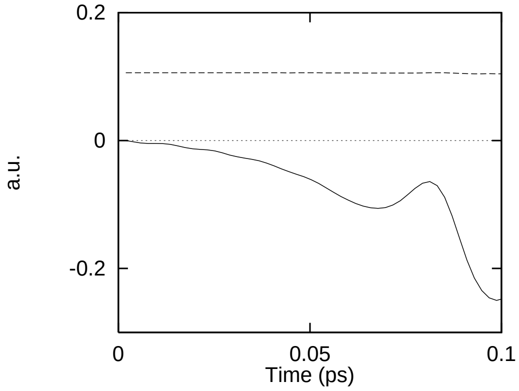

(b) Bridge, energies

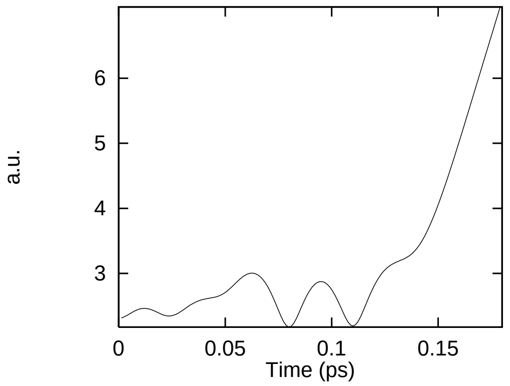

(c) On-top, O-O distance

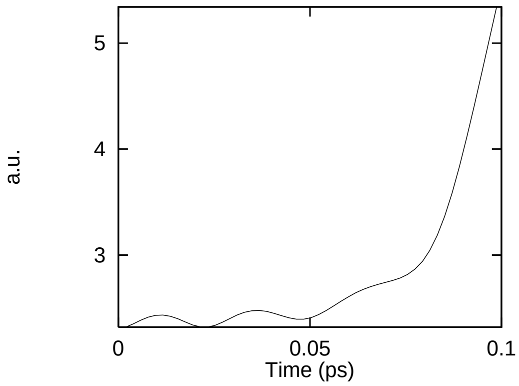

(d) Bridge, O-O distance

Figure 2.12: a) and b) BO ionic potential (full lines) and total energy (dashed lines); c) and d) O−O distance, as function of time, for the two trajectories of Fig. 2.11.

a constant, and this is a test on the goodness of our simulations. A detailed study of the modification of the dissociation barrier induced by the surface and of the kinetics of the dissociation is beyond the scope of this work. For the time being, we content ourselves with the qualitative agreement between this simulation and experimental findings, and we pass to a detailed study of the equilibrium adsorption sites and of the adsorption-induced reconstruction of the surface.

2.5.1 Structural properties

In Fig. 2.13 we display the three possible surface sites investigated in this work. In Table 2.3 we summarize the results of our calculations for $\Theta = \frac{1}{2}$. We see that the *on-top* and the *bridge* sites have an energy which is respectively 1.5 and 0.3 eV/atom higher than that of the *hollow* site, which is therefore the predicted stable adsorption site. The work function is larger at coverage $\Theta = \frac{1}{2}$ than for the clean surface, indicating that electrons tend to transfer from the substrate to the oxygen layer, thus increasing the surface dipole.

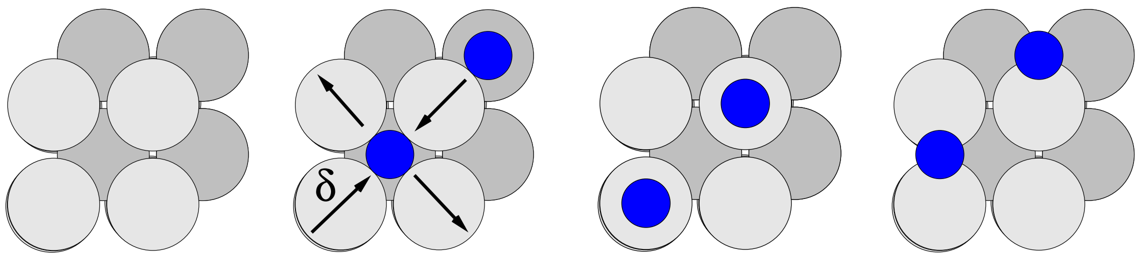

(a) clean (b) hollow (c) on-top (d) bridge

Figure 2.13: (Color) Sketch of the various O adsorption sites of the Rh(001) surfaces considered in this work. Small dark circles: O atoms. Large lighter circles: first-layer Rh atoms. Large darker circles: second-layer Rh atoms. The arrows indicate how the substrate atoms move after the distortion, δ is the amount of the shift.

The *hollow* site on the undistorted Rh(001) surface is a saddle point. If we reduce the symmetry of the system and we artificially distort the substrate as indicated in

unit	δ/d_0 %	d_{01} Å	d_{12}/d_0 %	ϕ (eV)	$E - E_{Hollow}$ (eV/atom)
Top		1.81	+3	7.5	+1.5
Bridge		1.33	+0.5	6.8	+0.3
Hollow		1.02	+0.5	6.2	0.0
Symmetric clock	$\approx$ 4	1.02	+0.5	6.2	−0.003
Asymmetric clock	$\approx$ 11	$0.98 \div 1.06$	$+0.5 \div 0.1$	6.1	−0.030
Expt.	$\approx 10^a$	0.95 ± 0.04^b	-0.5 ± 1.0^b		

[a] From Ref. [28], [b] From Ref. [69].

Table 2.3: Structural data for the three oxygenated structures investigated (see Fig. 2.13). The coverage is $\Theta = \frac{1}{2}$. d_0 is the bulk lattice spacing, d_{01} is the distance between the oxygen atoms and the first rhodium layer, d_{12} the distance between the first and the second layer. For the distorted structure the two given numbers refer to the two inequivalent first layer rhodium atoms (see Fig. 2.14). δ is the amplitude of the movement of the first-layer rhodium atoms upon distortion (see Fig. 2.13(b)), ϕ is the work function.

Fig. 2.10a, we find that this is an unstable configuration and the forces acting on the atoms restore the more symmetric c(2×2) structure. If instead we distort the substrate as indicated in Fig. 2.10b, we find that the slab relaxes so as to accommodate the distortion which brings two rhodium atoms at opposite corners of a 'black' square closer to the center occupied by an oxygen atom. We call this structure a 'symmetric clock' reconstruction. However, we find that this tendency can be further enhanced by lowering the symmetry of the surface and allowing the O atoms to get off the center of the rhombii formed by the four neighboring Rh atoms: this results in an 'asymmetric clock' reconstruction. This structure is displayed in Fig. 2.14. The substrate reconstruction is the same as the previous one, but in this case the oxygens do not stay in the middle of the *bridge* but move away in the orthogonal direction, becoming essentially *threefold* coordinated. The atomic rows of the first Rh layer are no longer equivalent to each other: every second row is made of atoms which have 2 oxygen neighbors, while the others have only 1 neighbor. As

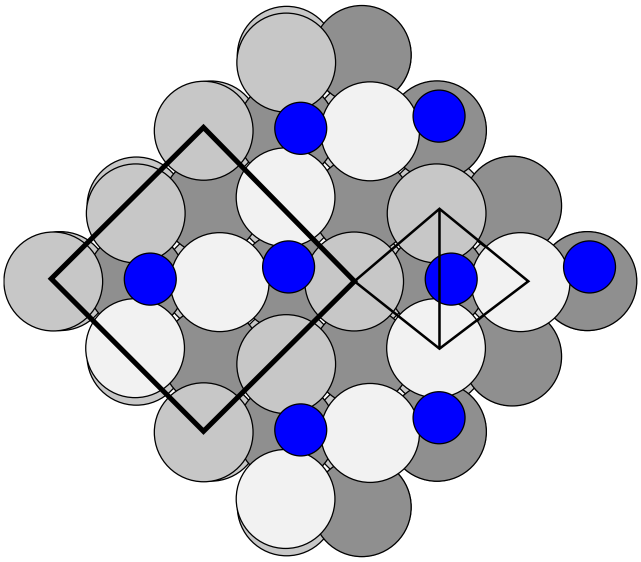

Figure 2.14: (Color) The oxygenated Rh(001) surface after a simulated annealing run. The unit cell is indicated with the thick line. The thin line indicates the rhombus and its shorter diagonal, the *bridge*. The oxygen atoms are alternatively shifted orthogonally with respect to the *bridge*. The brighter atoms of the first surface layer are ≈ 0.08 Å higher then the others.

a consequence the first rhodium layer results to be buckled, the 2-fold coordinated rows leaning ≈ 0.08 Å outwards. The stability of this minimum has been checked by a simulated annealing procedure.

From Fig. 2.14 it is evident that the oxygen sub-lattice is in a 'zig-zag' arrangement which is not observed in the experiments. However, there are two equivalent threefold sites per cell for each oxygen atom, one on each side of the bridge. Neglecting the interactions between different adsorption sites, each of them is therefore two-fold degenerate. This fact implies that at high temperature the oxygen sub-lattice would be disordered. At low temperature it could be ordered, but with our small cell only one (ordered) configuration is possible. From STM images no ordered oxygen ad-layer is detected. This fact has two consequences: the first one is that the temperature at which the STM measurements have been performed (room temperature) is higher than the critical one; the second consequence is that the frequency of oxygen barrier crossing is much larger than the scanning frequency of

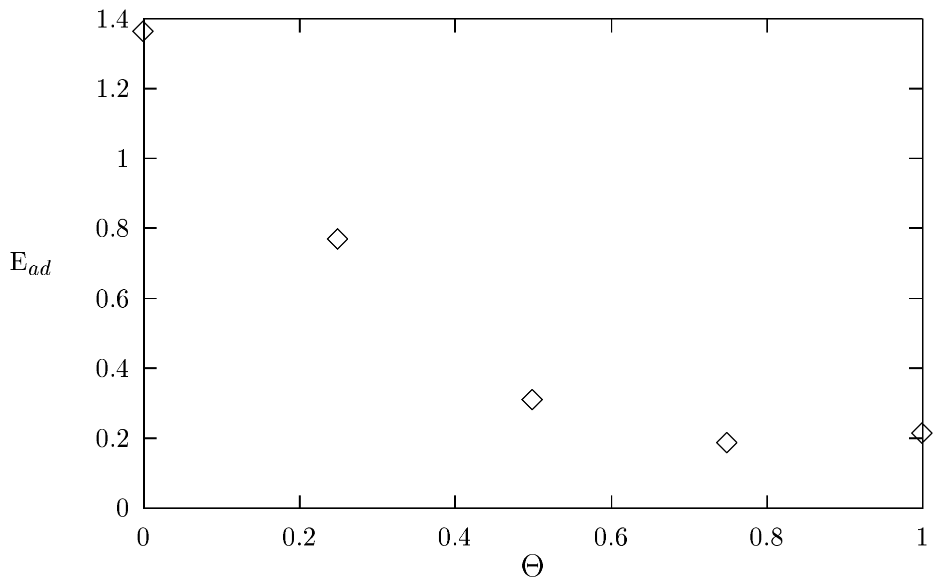

Figure 2.15: The oxygen adsorption energy as a function of coverage.

the STM. This is compatible with our estimates of the barrier height (≈ 30 meV, as obtained by comparing the energies of the 'symmetric clock' and the 'asymmetric clock' structures) which is of the order of the room temperature.

In Fig. 2.15 we display the adsorption energy, E_{ad} as a function of coverage, Θ, defined as:

$$E_{ad}(\Theta) \;=\; \sigma(\Theta) \;-\; \sigma(0) \;-\; \frac{\Theta}{2} E_{\mathrm{O}_2}, \qquad (2.9)$$

where $\sigma(\Theta)$ is the surface energy of the oxygen-covered system, and E_{O_2} is the energy of the isolated O_2 molecule, estimated using local spin density approximation (LSDA) for the exchange and correlation energy. Coverage $\Theta = 1$ is realized filling all the square sites, $\Theta = 0.75$, and $\Theta = 0.25$ filling respectively 3 and 1 of the 4 possible square sites in a 2×2 substrate super-cell. The minimum energy corresponds to a coverage in the range $\frac{1}{2} \leq \Theta \leq 1$. In this range, however, the curve is very flat and the variation of the adsorption energy (< 0.1 eV) is smaller than the expected accuracy of the terms which enter its definition. All we can safely predict is that the stable coverage state lies somewhere in between $\Theta = \frac{1}{2}$ and $\Theta = 1$. The value of the most stable coverage is determined by a trade-off between the adsorption energy of an isolated oxygen molecule, which tends to favor a high coverage, and the oxygen-oxygen repulsion which becomes more effective when the average $\mathrm{O}-\mathrm{O}$ distance becomes smaller than some typical screening length, and which tends instead to favor a low coverage.

In the following we discuss the mechanism of the 'clock' reconstruction of the O/Rh(001) system in terms of simple chemical concepts based onto the atomic orbitals involved in the oxygen-surface bond. Our discussion is limited to the 'symmetric clock' reconstruction, but we believe that our conclusions are of general validity and also apply to the more stable 'asymmetric clock' reconstruction. In Fig. 2.16 we display the surface-projected densities of states (SDOS) [3] of the clean and of the oxygen-covered Rh(001) surface, along with their decompositions into various atomic-like contributions. The SDOS of the clean surface is almost entirely entirely determined by its d-like component (see Fig. 2.16a) and it is very similar to its bulk counterpart, which is broader because of the larger coordination number in the bulk with respect to the surface. In the bulk FCC structure the three d_{xy}, d_{xz} and d_{yz} are degenerate, and so are $d_{3z^2-r^2}$ and $d_{x^2-y^2}$. This degeneracy is partially lifted at the surface. For the (001) surface, the d_{xz} and d_{yz} orbitals are still equivalent by symmetry and, hence, degenerate. The position of the oxygen atomic p-level is about 3.1 eV below the Fermi energy of the oxygen-covered surface. Inspection of Fig. 2.16d shows that the $\mathrm{O}_{p_x} = \mathrm{O}_{p_y}$ level gives rise to a bonding and an anti-bonding main peaks, respectively below (-5.8 eV) and above ($+1$ eV) the Fermi level. Upon oxygen adsorption, first-layer Rh atoms become locally inequivalent according to whether the neighboring oxygen atoms are aligned along the x or y directions (see Fig. 2.16e). PDOS plotted in Fig. 2.16d refers to those Rh atoms which have O neighbors aligned along the y direction (the PDOS of the other Rh atoms can be obtained by simply exchanging x with y). It is also easy to recognize that the same bonding and anti-bonding features occur in the d_{yz} band whose atomic orbitals

[3] We define the surface-projected densities of states as the sum over all the surface PDOS's defined in Eq. 2.2.

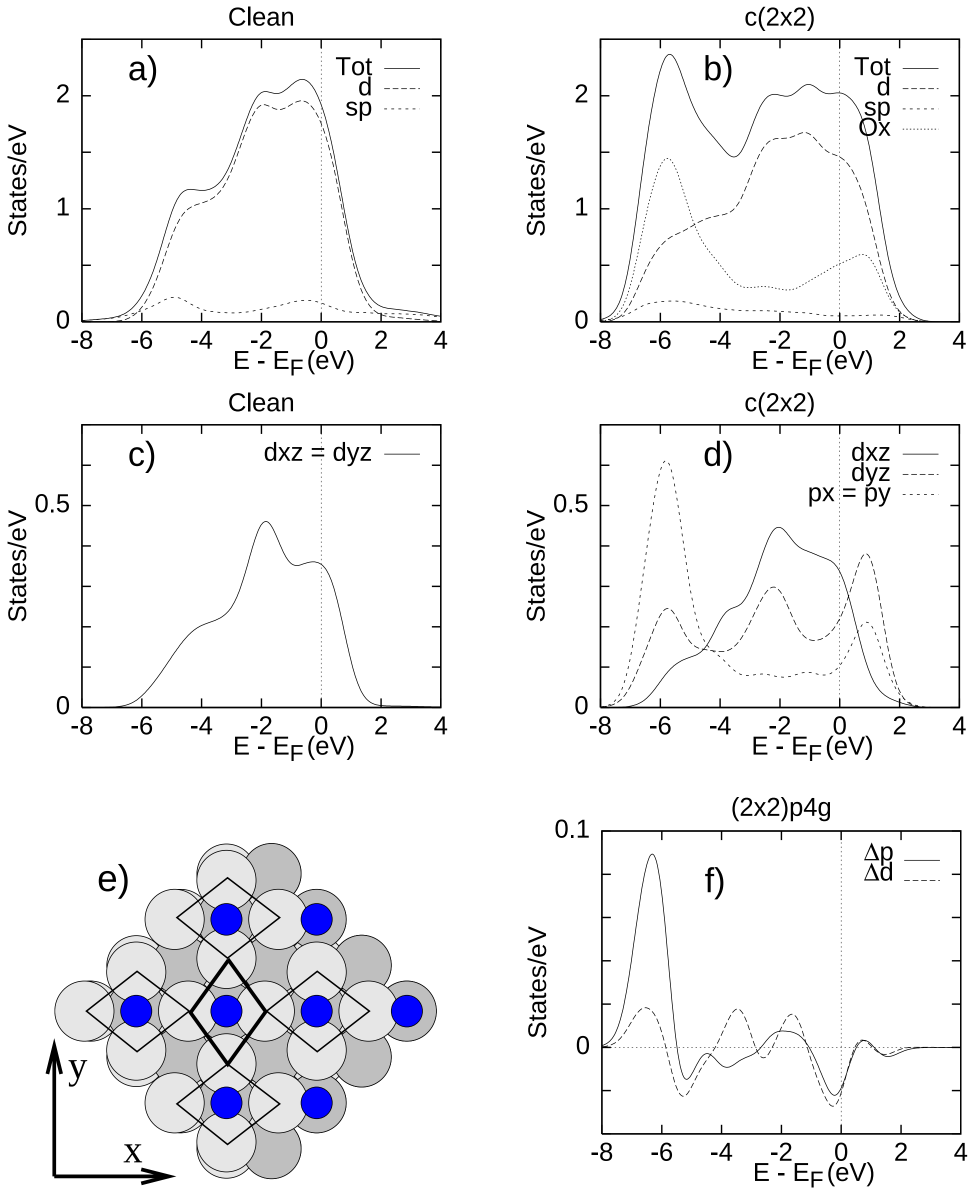

Figure 2.16: (Color) *a)* SDOS of the clean Rh(001) surface; *b)* SDOS of the oxygen covered Rh(001) surface; *c)* Projection of the SDOS onto the $d_{xz} = d_{yz}$ first-layer rhodium orbitals for the clean surface; *d)* Projection of the SDOS onto the $p_x = p_y$ oxygen orbitals and of d_{xz} and d_{yz} first-layer rhodium orbitals for oxygenated, unreconstructed, surface; *e)* Sketch of the (2×2)p4g, *clock*, reconstruction. The amplitude of the deformation is exaggerated for clarity; *f)* Differences between the O_p- and Rh_d-projected density of states in the reconstructed and unreconstructed structures.

have lobes oriented towards the adsorbed oxygen, while the d_{xz} band remains similar to that of the clean surface (see Fig. 2.16c) because in that direction the surface sites are empty. The O_{p_x} orbitals make bonds with the d_{xz} orbitals of the Rh atoms along the x direction, while the O_{p_y} orbitals hybridize with the d_{yz} orbitals of the Rh atoms along the y direction.The (2×2)p4g reconstruction shortens and strengthens the O$-$Rh bonds along one direction, while lengthening them in the perpendicular direction, as illustrated in Fig. 2.16e. The amplitude of the distortion (δ/d_0 see Fig. 2.13) depends rather sensitively on the lattice parameter: using our calculated lattice parameter, we estimate the distortion to be $\approx 4\%$; if we use a lattice parameter 1% larger, the amplitude of the distortion also is increased, reaching a value $\approx 6\%$. The opposite occurs if the lattice parameter is reduced. The tendency of the system to strengthen two of the four rhodium bonds at the expenses of the other two results in a net lowering of the surface energy of ≈ 3 meV/atom, thus stabilizing the (2×2)p4g structure. In the 'asymmetric clock' more stable structure the amount of the distortion is $\approx 11\%$ (using our calculated lattice parameter) and the surface energy gain is ≈ 30 meV/atom. This shows that the reconstruction occurs because the optimal O$-$Rh bond-length is shorter than that realized in the ideal geometry. The 'chemical' contribution to the energy lowering which determines the distortion is illustrated in Fig. 2.16f which shows the differences between the Rh_d and O_p PDOS after and before the reconstruction. In both cases, we notice that electronic states are pushed towards lower energies.

2.5.2 Related systems: C/Ni(001), N/Ni(001), O/Ni(001)

As it was mentioned in the introduction, a reconstruction similar to the one described in the previous section is observed for nitrogen and carbon adsorbed on the (001) surface of nickel. In that case, however, the rotation angle of the squares is much larger and the 'clock' reconstruction is more evident [29, 30, 31, 32, 33]. Moreover, the additional LEED I-V data for C/Ni(001) [32] and SEXAFS data for N/Ni(001) [33] allow a more precise identification of the reconstruction which is reported to

Configuration	$3d$	$\Delta(3d)$	$4s$	$\Delta(4s)$	$4p$	$\Delta(4p)$
$[Ar]3d^8 4s^2 4p^0$	-0.67163	0.0	-0.43114	0.0	-0.09863	0.0
$[Ar]3d^8 4s^1 4p^1$	-0.81217	-3.7	-0.52244	-0.5	-0.16628	0.0
$[Ar]3d^7 4s^2 4p^1$	-1.20891	8.3	-0.60788	-2.7	-0.20263	4.9
$[Ar]3d^8 4s^1 4p^0$	-1.34216	3.1	-0.99314	1.2	-0.57324	1.6
$[Ar]3d^7 4s^2 4p^0$	-1.78628	26.0	-1.12276	4.1	-0.65965	12.4
$[Ar]3d^8 4s^0 4p^0$	-2.10990	5.2	-1.60533	4.6	-1.10670	7.3

Table 2.4: Transferability of the nickel pseudopotential. All electron $3d$, $4s$, and $4p$ eigenvalues are given in Rydbergs, the differences Δ in mRydbergs.

be of type 'black' (i.e. it is the squares occupied by one adsorbed atom which rotate). Oxygen adsorption does not induce any 'clock' reconstruction on Ni(001). In this case the only effect that has been observed is a buckling reconstruction in the second nickel layer, which are not all coplanar but shifted 'up' or 'down' according to whether the fourfold site lying above is empty or filled [70, 71].

In the following we report on some preliminary results we have obtained for the C/Ni(001), N/Ni(001), and O/Ni(001) systems.

Nickel

The nickel pseudopotential has been constructed treating the d channel in the ultrasoft scheme, while the s and the p channels are norm-conserving. The core radii are respectively 1.76, 1.22 and 1.77 a.u. for the $3d$, $4s$ and $4p$ states. The reference configuration is the $3d^8 4s^2 4p^0$ and the local part of the PP has been chosen to be the $l = 1$ component, which avoids the appearance of *ghost* states. The value of the core radii has been chosen in order to minimize the mean square difference among the AE and the PP eigenvalues for six different configurations (see Table 2.4).

Nickel bulk has the FCC crystal structure. To calculate the equilibrium lattice constant a_0 and the bulk modulus B_0, we have fitted to the Murnaghan's equation of state (Eq. 2.1) the calculated energies as a function of the unit cell volume.

We have used PW's up to a maximum kinetic energy of 30 Ry and we have found converged structural properties using 10 MP **k**-points in the IBZ and a smearing function of order 1 with a width of $\sigma = 0.03$ Ry. The calculated lattice constant is $a_0 = 3.44$ Å and the bulk modulus is $B_0 = 2.4$ Mbar, to be compared with the experimental values, $a_0 = 3.52$ Å and $B_0 = 1.73$ Mbar [54]. Nickel bulk is magnetic with a magnetic moment of 0.59 μ_B/atom [72]. An explicit account of the spin polarization at the LSDA level did not result in any meaningful changes of the structural properties calculated within the LDA. The magnetism is expected to be more important at the surface, because the surface density of states is narrower then the bulk one. However, at least for the carbon and the nitrogen covered surfaces, we have found that the Ni-d-SDOS is shifted towards lower energies with respect to the bulk d-PDOS (see Fig. 2.17) thus resulting in a lower DOS at the Fermi level. We argue that magnetic effects should not be very important and therefore they have been neglected altogether in the present investigation.

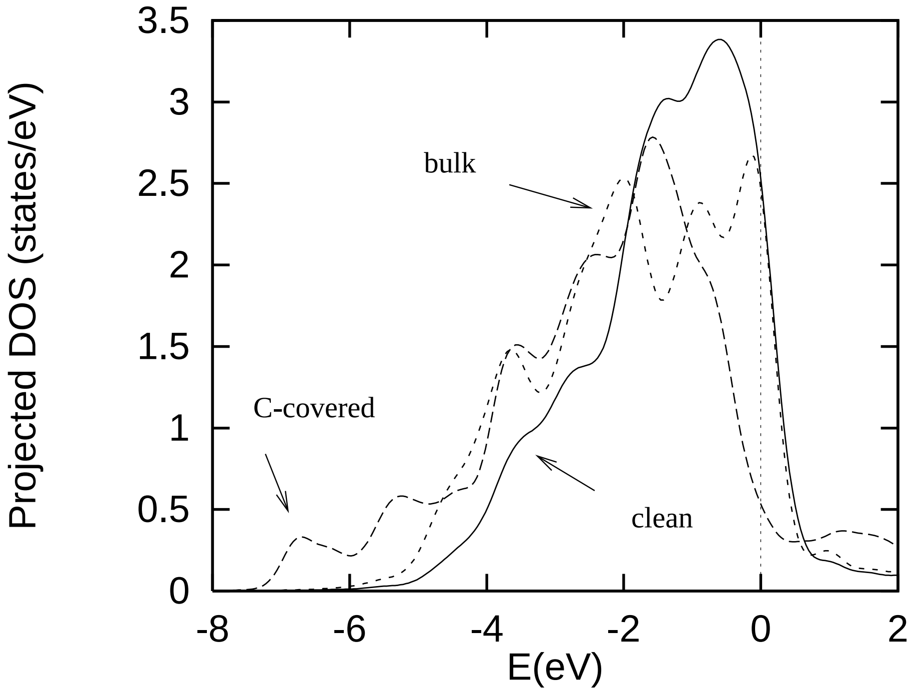

Figure 2.17: d-projected density of states of nickel for the bulk, the clean surface, and the carbon-covered surface.

Results

In order to find the stable surface structure of the C/Ni(001), N/Ni(001) and O/Ni(001) systems we have performed simulated annealing runs of the surfaces at half monolayer of coverage. For the carbon and nitrogen covered surface we have found a surface reconstruction where it is the *filled* squares which rotate ('black' reconstruction see Fig. 2.10a), at variance to what we have found for the oxygenated Rh(001) surface, and in agreement with the experimental findings [32, 33]. In the case of carbon we have found the reconstruction even with a direct relaxation of the slab, while for the nitrogen covered surface the system remains trapped in a meta-stable unreconstructed structure and an annealing is necessary to overcome the energy barrier and reach the most stable reconstructed one. At variance with the rhodium case where the oxygen distance from the surface is not appreciably different in the distorted and undistorted case, on the nickel surface we have found that the carbon and the nitrogen atoms are almost coplanar with the substrate ones, in agreement with Refs. [30, 31].

For the O/Ni(001) system we have not found any reconstruction at all, and also this fact is in agreement with the experimental data [69]. The behaviour of the oxygen on the two surfaces is consistent with our interpretation for the O/Rh(001) reconstruction. The nickel lattice parameter in fact is quite smaller then the rhodium one, and therefore the nickel site is already "small enough" for the oxygen ad-atoms.

The behaviour of the two surfaces (Ni(001) and Rh(001)) is apparently very similar (they have the same STM images and LEED patterns) but they are different as regards the chemical bonds they form with carbon, nitrogen, and oxygen adsorbates, which induce on Ni(001) and Rh(001) respectively two different reconstructions. The mechanism proposed for the rhodium reconstruction cannot be transferred to the case of nickel, where the ad-atom sites remain squares after the reconstruction.

In Table 2.5 we report a summary of the main structural properties of these four systems investigated.

	Expt.	Theory	Expt.	Theory	Expt.	Theory	Theory
	Reconstruction		δ/d_0		d_{01}		ΔE
unit			%		Å		eV/atom
C:Ni	a	a	$\approx 40^a$	≈ 27	0.1 ± 0.1^b	0.17	0.20
N:Ni	a	a	$\approx 30^c$	≈ 24	0.11 ± 0.06^c	0.10	0.08
O:Ni	none	none			0.77 ± 0.04^d	0.73	
O:Rh	?	b	≈ 10	≈ 11	0.95 ± 0.04^e	$0.98 \div 1.06$	0.03

^{b} From Ref. [32], ^{b} From Ref. [30], ^{c} From Ref. [31], ^{d} From Ref. [69], ^{e} From Ref. [70].

Table 2.5: Summary of the structural data for the four systems investigated. For the reconstruction type see Fig. 2.10. d_0 is the bulk lattice spacing, d_{01} is the distance between the adsorbate atoms and the first metal layer, in the case of O:Rh the two numbers are the distances of the oxygen from the 'bright' and the 'dark' first layer rhodium rows (see Fig. 2.14). d_{12} is the distance between the first and the second layer, δ is the amplitude of the movement of the first-layer metal atoms upon distortion and ΔE is the energy difference per atom between the symmetric c(2×2) structures and the reconstructed ones.

2.5.3 Scanning tunneling microscope images

The experimental data which show the reconstruction of the Rh(001) surface upon oxygen adsorption are based on LEED and STM observations.

In the lower panels of Fig. 2.19 we display the calculated STM images of the oxygenated Rh(001) surface for positive and negative bias of the sample respectively, in the upper panels the corresponding experimental ones [28].

Our images are calculated in the spirit of the Tersoff and Hamann approximation [73]. Essentially, the intensity I of the tunneling current is proportional to the local density of states at the Fermi energy of the sample,

$$I \propto \sum_{n\mathbf{k}} |\psi_{n\mathbf{k}}(\mathbf{r})|^2 \delta(E_{n,\mathbf{k}} - E_F), \tag{2.10}$$

where $\psi_{n\mathbf{k}}(\mathbf{r})$ is the sample wave-function, $E_{n,\mathbf{k}}$ its energy, E_F is the Fermi energy of the sample, and $\mathbf{r}$ is the position of the tip. When the sample is biased, the position

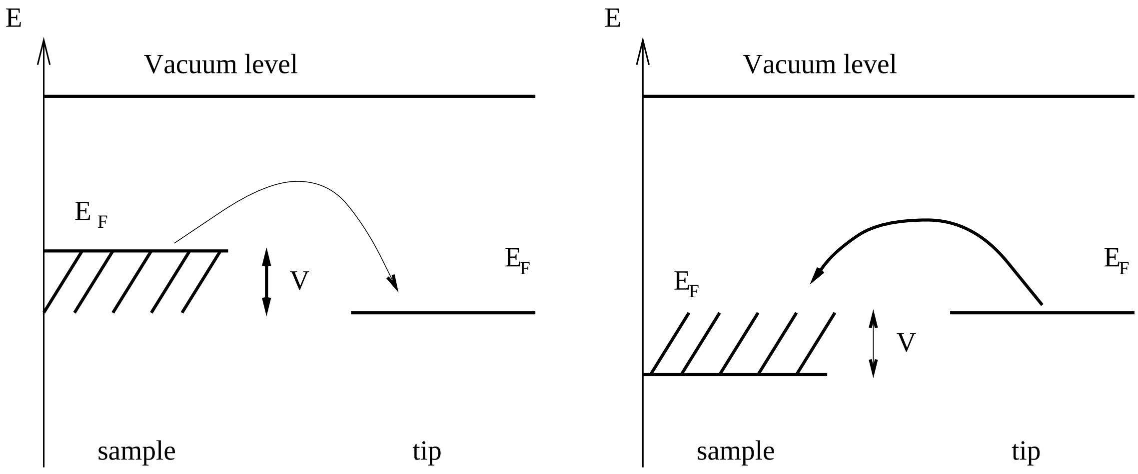

(a) Negative bias (b) Positive bias

Figure 2.18: Sketch of the tunneling current for the case of negative *(a)* and positive *(b)* biased sample.

of its Fermi level with respect to the vacuum level is shifted by the amount of the biasing potential (see Fig. 2.18). If the bias is negative and the tip is grounded, then the sample Fermi energy is shifted upward, the electrons flow from the *filled* state of the sample into the tip and then the *filled* stated are imaged. If instead the bias is positive the opposite happens, the electrons flow from the tip into the *empty* states of the sample and then are these states to be imaged.

The Tersoff and Hamann approximation has been implemented as in Ref. [74]. A direct use of the self-consistent KS eigenfunctions does not allow the calculation of images at a distance from the surface larger then one half of the thickness of the vacuum region in the super-cell. Moreover, far from the surface the wave-functions are not well described, since the finiteness of the cutoff energy is not able to describe in an accurate way their exponential tails. However, the exact form of the tails of the wave-functions in the vacuum region is known:

$$\psi_{n\mathbf{k}}(\mathbf{r}) = \Omega^{-\frac{1}{2}} \sum_{\mathbf{G}_{\parallel}} a_{\mathbf{G}_{\parallel}} e^{-(\kappa^2+|\kappa_{\mathbf{G}_{\parallel}}|^2)^{\frac{1}{2}} z} e^{i\kappa_{\mathbf{G}_{\parallel}}\cdot\mathbf{x}}, \tag{2.11}$$

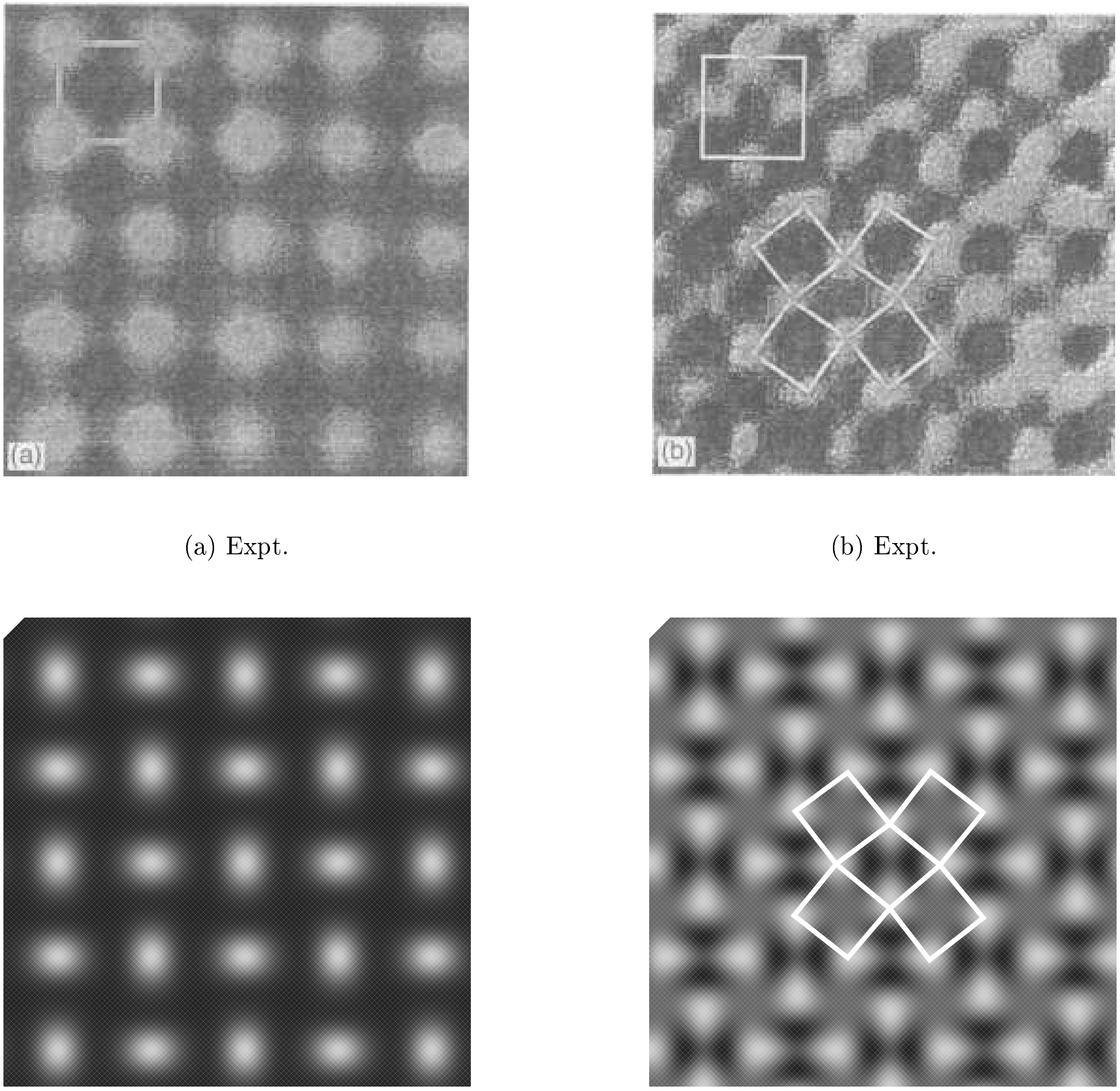

(a) Expt.

(b) Expt.

(c) Theory

(d) Theory

Figure 2.19: (a) and (b) Experimental STM images of the $(2 \times 2)p4g$ phase of O on Rh(001) (19×19 Å^2, sample bias 0.1 mV, tunneling current 3 nA). In (a) the oxygen atoms are imaged as protrusions while in (b) as depressions [28]. (c) and (d) Calculated STM images of the same surface at ≈ 2 Å from the surface. In (c) the sample bias is $+13$ mV and the oxygen atoms are imaged as protrusions, in (d) the sample bias is -13 mV and the oxygen atoms are hidden, the rhodium substrate is imaged.

where $\kappa = \hbar^{-1}(2m\phi)^{\frac{1}{2}}$, ϕ is the work function, $\kappa_{\mathbf{G}_\parallel} = \mathbf{k}_\parallel + \mathbf{G}_\parallel$, $\mathbf{G}_\parallel$ is a surface reciprocal lattice vector and $\mathbf{k}_\parallel$ is the surface Bloch wave vector of the state, z is the distance from the surface along its normal and $\mathbf{x}$ is the vector in the surface plane. Far from the surface one can thus replace the KS eigenfunction with the form 2.11, once the coefficients $a_{\mathbf{G}}$ are known. These can be determined by matching the expression 2.11 with the KS wave-functions

$$\psi_{n\mathbf{k}}(\mathbf{r}) = \Omega^{-\frac{1}{2}} \sum_{\mathbf{G}_\parallel, g_z} b_{\mathbf{G}_\parallel, g_z} e^{i g_z z} e^{i\kappa_{\mathbf{G}} \cdot \mathbf{x}}, \qquad \mathbf{G} = (\mathbf{G}_\parallel, g_z), \tag{2.12}$$

at a point z_0 where both the expressions 2.11 and 2.12 give a good description of the surface wave-functions. To calculate the positive biased images, states in the window $(E_F, E_F + V)$ are taken into account, while for negative bias the window of states is (E_F+V, E_F), the work function is correspondingly modified, $\phi \to \phi - V - (E_{n,\mathbf{k}} - E_F)$, in both cases.

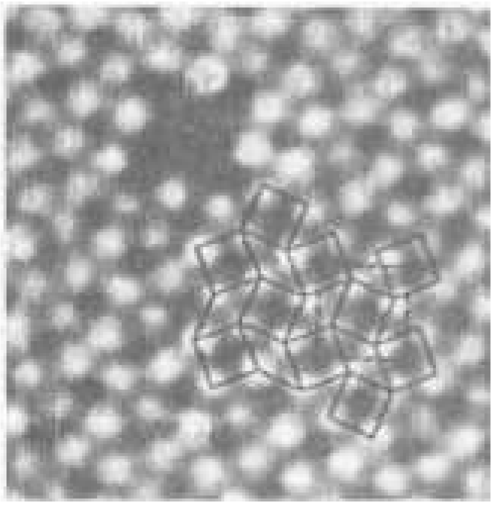

(a) Expt.

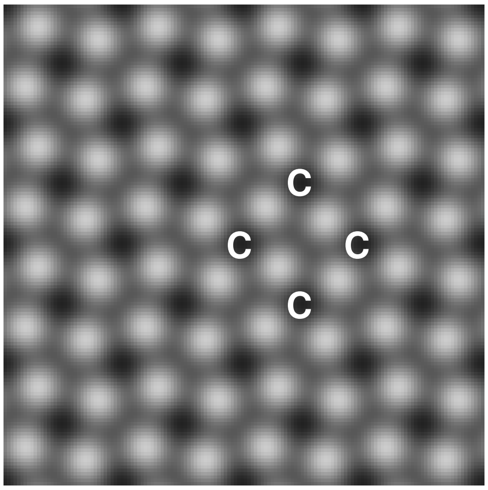

(b) Theory

Figure 2.20: (a) Experimental STM images of the $(2 \times 2)p4g$ phase of C on Ni(001) (28×28 Å^2, sample bias 10 mV, tunneling current 0.61 nA)[30]. (b) Calculated STM images of the same surface at ≈ 4 Å from the surface (19×19 Å^2, sample bias $-.13$ V the carbon atoms are hidden, the nickel substrate is imaged).

In Fig. 2.19 we display the STM images as obtained from experiments [28] (upper panels) and from our calculations using Eq. 2.10 (lower panels). In the case of positive bias of the sample (tunneling from the tip into the sample) only the oxygen is imaged, and this is consistent with the form of the PDOS for the oxygen p orbitals, which have an anti-bonding feature just above the Fermi energy (see Fig. 2.16). In the case of negative bias, instead, the oxygen is hidden and the substrate rhodium atoms are imaged, again, this is consistent with the form of the PDOS for oxygen and rhodium just below the Fermi energy.

Our calculated STM images are similar to the experimental ones, but at variance with Ref. [28] we identify the oxygen position is in the center of the *rhombii*.

In Fig. 2.20 we display the experimental (left panel) and the calculated (right panel) STM images for the Ni(001)-(2×2)p4g-C surface: the images are very similar. However, as in the case of rhodium, the adsorbate is hidden, and the carbon atoms are in the center of the squares. For this reason, STM images are not sufficient to identify which of the possible two reconstructions is actually present.

Conclusions

This thesis is a contribution to the study of the elementary steps of the catalytic reaction $2CO + 2NO \rightarrow 2CO_2 + N_2$, which occurs in the proximity of some transition metal surfaces, such as rhodium or platinum. We have concentrated on two particular problems: the first one is the structure and phase stability of CO adsorbates on the Rh(110) surface. We have confirmed the experimental claims of an order-disorder transition of the CO ad-layer, occurring at a temperature just below the desorption temperature [15]. The transition is not easily characterized in the experiments because of the proximity between the critical and the desorption temperatures. Our study has revealed the microscopic mechanisms responsible for the order-disorder transition, and indicated that it is second-order. The other problem we have studied is the adsorption of oxygen on the Rh(001) surface on which ad-atoms occupy every second cell of the surface lattice. In agreement with experiments, we have found that the substrate undergoes a reconstruction in which every second square cell is distorted to a rhombus. We identify the squares which distort as those occupied by an ad-atom, at variance with the current interpretation of existing experimental STM data [28]. Our conclusions, even if in disagreement with this interpretation, are substantiated by a simple chemical model of O–Rh rebonding at the surface. Furthermore, similar calculations performed for C/Ni(001) and N/Ni(001)—where an analogous reconstruction is also observed and much better characterized [32, 33]—are in very good agreement with experimental findings, thus giving us further confidence in their predictive power. In spite of the analogies existing between the reconstruction of O/Rh(001) and those of C/Ni(001) and

N/Ni(001), we find that their nature is unsuspectedly rather different. The carbon atoms penetrate into the nickel substrate even at zero temperature, and they arrange themselves so as to be almost coplanar with the first nickel layer; the nitrogen atoms behave similarly but a barrier is found to exist, which gives rise to a metastable equilibrium structure in which the ad-atoms do not penetrate and the surface does not reconstruct. These facts indicate that the mechanism of the reconstruction is related with the atomic penetration into the first surface layer: the sites which accommodate the ad-atoms must enlarge and this results necessarily in a rhomboid distortion of the others. In the case of the oxygen the mechanism of the reconstruction is completely different, being due to the O–Rh re-bonding, thus resulting in a different reconstruction pattern. At the time of the writing of this thesis, further calculations aiming at clarifying the different behaviour of C, N and O on Rh(001) and Ni(001) are being done. Our results for O/Rh(001) point to a second problem that is still opened. The equilibrium structure we find for this system has a lower symmetry than the c(2×2) observed experimentally, compatibly with the existence of an order-disorder transition below the temperature at which the STM images have been taken (room temperature). Additional work is required to support this suggestion.

The comprehension of the catalytic reaction described above is far to be complete. The investigation of many related problems is still going on. A complete simulation of the whole reaction from *first principles* is a difficult task. Many atoms should be included in the system and, even more important, the characteristic times are too large to be explored. However, using the new tools we have developed in this thesis, such as the inclusion of molecular dynamics in our DFT-LDA code and, particularly, constrained structure optimization, we are ready to undertake more ambitious studies of some simple single steps of the reaction. For example the kinetics of the NO dissociation is not yet clear, and a study of the dissociation barriers is a problem which can be studied in the immediate future.

Appendix A

Diagonalization

A.1 Conjugate gradient diagonalization

The problem is: minimize [1]

$$f_j = \frac{1}{2}\langle\psi_j|H|\psi_j\rangle \tag{A.1}$$

under the constraints:

$$\langle\psi_j|S|\psi_j\rangle = 1, \qquad \langle\psi_j|S|\psi_k\rangle = 0, \quad k < j. \tag{A.2}$$

This is equivalent to solve the Euler-Lagrange problem of minimizing

$$\widetilde{f}_j = \frac{1}{2}\langle\psi_j|H|\psi_j\rangle - \epsilon_j(\langle\psi_j|S|\psi_j\rangle - 1) - \sum_{k<j}\lambda_{jk}\langle\psi_j|S|\psi_k\rangle. \tag{A.3}$$

If we consider the gradient of the expression above we have:

$$|g_j\rangle = H|\psi_j\rangle - \epsilon_j S|\psi_j\rangle - \sum_{k<j}\lambda_{jk}S|\psi_k\rangle \tag{A.4}$$

but we are not able to find a simple expression for ϵ_j and λ_{jk} in order to have $\langle g_j|S|\psi_k\rangle = 0$ because $\langle\psi_j|S^2|\psi_k\rangle \neq 0$. So we use a slightly different approach: we firstly consider only the first constraint. The problem is equivalent to the minimization of

[1]The original formulation of these notes, for the problem without the overlap matrix S, is due to Paolo Giannozzi.

$$\widetilde{f}_j \;=\; \frac{1}{2}\langle\psi_j|H|\psi_j\rangle \;-\; \epsilon_j(\langle\psi_j|S|\psi_j\rangle \;-\; 1). \tag{A.5}$$

First step. For any given index j we assume a starting vector $|\psi_j^0\rangle$ such that

$$\langle\psi_j^0|S|\psi_j^0\rangle \;=\; 1, \qquad \langle\psi_j^0|S|\psi_k\rangle \;=\; 0, \quad k<j. \tag{A.6}$$

The gradient $|g_j^0\rangle$ is

$$|g_j^0\rangle \;=\; H|\psi_j^0\rangle \;-\; \epsilon_j^{0^*}S|\psi_j^0\rangle \tag{A.7}$$

where

$$\epsilon_j^{0^*} \;=\; \frac{\langle\psi_j^0|SH|\psi_j^0\rangle}{\langle\psi_j^0|S^2|\psi_j^0\rangle} \tag{A.8}$$

ensures that $\langle g_j^0|S|\psi_j^0\rangle = 0$. We also define:

$$\epsilon_j^0 \;=\; \langle\psi_j^0|H|\psi_j^0\rangle \tag{A.9}$$

which is an approximation for the true eigenvalue ϵ_j of H. The second set of constraints is accounted requiring that

$$\langle g_j^0|S|\psi_k\rangle \;=\; 0. \tag{A.10}$$

This is obtained by an explicit Gram-Shmidt orthogonalization, with the overlap matrix S, of $|g_j^0\rangle$ to $|\psi_k\rangle, k<j$

$$|g_j^0\rangle \;=\; H|\psi_j^0\rangle \;-\; \epsilon_j^{0^*}S|\psi_j^0\rangle \;-\; \sum_{k<j}\lambda_{kj}^0|\psi_k\rangle \tag{A.11}$$

where

$$\lambda_{kj}^0 \;=\; \langle g_j^0|S|\psi_k\rangle. \tag{A.12}$$

Note that Eq. A.11 is different from Eq. A.4, the last term of the right hand side is $\sum_{k<j}\lambda_{kj}^0|\psi_k\rangle$ instead of $\sum_{k<j}\lambda_{kj}^0 S|\psi_k\rangle$.
Now: let us consider the conjugate direction $|h_j^0\rangle = |g_j^0\rangle$ and the normalized direction $|\widetilde{h}_j^0\rangle$:

$$|\widetilde{h}_j^0\rangle \;=\; \frac{|h_j^0\rangle}{\langle h_j^0|S|h_j^0\rangle^{1/2}}. \tag{A.13}$$

By construction

$$\langle\widetilde{h}_j^0|S|\widetilde{h}_j^0\rangle \;=\; 1, \quad \langle\widetilde{h}_j^0|S|\psi_j^0\rangle \;=\; 0, \quad \langle\widetilde{h}_j^0|S|\psi_k\rangle \;=\; 0 \quad . \tag{A.14}$$

Consider the vector

$$|\psi_j^1(\theta)\rangle \;=\; \cos\theta|\psi_j^0\rangle \;+\; \sum_{i=1}^{N}\theta|\widetilde{h}_j^0\rangle. \tag{A.15}$$

By construction,

$$\langle\psi_j^1(\theta)|S|\psi_j^1(\theta)\rangle \;=\; 1, \qquad \langle\psi_j^1(\theta)|S|\psi_k\rangle \;=\; 0, \quad k<j. \tag{A.16}$$

We look for the value of θ that minimizes

$$\epsilon_j^1(\theta) \;=\; \langle\psi_j^1(\theta)|H|\psi_j^1(\theta)\rangle. \tag{A.17}$$

The solution is

$$\theta_j^0 \;=\; \frac{1}{2}\mathrm{arctag}\left(\frac{a_j^0}{\epsilon_j^0 \;-\; b_j^0}\right) \tag{A.18}$$

where

$$a_j^0 \;=\; \langle\psi_j^0|H|\widetilde{h}_j^0\rangle \;+\; c.c., \quad b_j^0 \;=\; \langle\widetilde{h}_j^0|H|\widetilde{h}_j^0\rangle \tag{A.19}$$

and

$$\epsilon_j^1 \;=\; \frac{\epsilon_j^0 \;+\; b_j^0 \;-\; \sqrt{(\epsilon_j^0 \;-\; b_j^0)^2 \;+\; (a_j^0)^2}}{2}, \tag{A.20}$$

which is a new approximation for ϵ_j.

Following steps. We construct the new gradient $|g_j^n\rangle$ as above and the new conjugate direction $|h_j^n\rangle$ as in the conjugate gradient method. We define

$$|u_j^n\rangle \;=\; |g_j^n\rangle \;+\; \gamma_j^{n-1}|h_j^{n-1}\rangle \tag{A.21}$$

$$\gamma_j^{n-1} \;=\; \frac{\langle g_j^n|S|g_j^n\rangle}{\langle g_j^{n-1}|S|g_j^{n-1}\rangle} \simeq \frac{\langle g_j^n - g_j^{n-1}|S|g_j^n\rangle}{\langle g_j^{n-1}|S|g_j^{n-1}\rangle}. \tag{A.22}$$

By construction,

$$\langle g_j^n|S|\psi_k\rangle \;=\; 0 \longrightarrow \langle u_j^n|S|\psi_k\rangle \;=\; 0 \tag{A.23}$$

but

$$\beta_j^n \;=\; \langle u_j^n|S|\psi_j^n\rangle \;=\; \gamma_j^{n-1}\langle h_j^{n-1}|S|\psi_j^n\rangle \;=\; \gamma_j^{n-1}\sum_{i=1}^{N}\theta_j^{n-1}\langle h_j^{n-1}|S|\widetilde{h}_j^{n-1}\rangle \neq 0 \tag{A.24}$$

so that explicit orthogonalization of $|\psi_j^n\rangle$ to $|u_j^n\rangle$ is needed (it is a consequence of the constraint of unitary norm):

$$|h_j^n\rangle \;=\; |u_j^n\rangle \;-\; \beta_j^n|\psi_j^n\rangle. \tag{A.25}$$

Then one proceeds as above, finds ϵ_j^n and checks if $|\epsilon_j^n - \epsilon_j^{n-1}| < tol$, where tol is a small number which defines the precision of ϵ_j, one can also check if $\langle g_j^n|g_j^n\rangle < tol'$, and in this case tol' defines the convergence of the eigenvectors.

Preconditioning

We define a (diagonal) preconditioning matrix P and auxiliary functions $|y\rangle$:

$$|y_j\rangle \;=\; P^{-1}|\psi_j\rangle. \tag{A.26}$$

One has to solve the equivalent problem of minimizing

$$f_j \;=\; \frac{1}{2}\langle y_j|(PHP)|y_j\rangle \tag{A.27}$$

under the constraints that

$$\langle y_j|(PSP)|y_j\rangle \;=\; 1, \qquad \langle y_j|PS|\psi_k\rangle \;=\; 0, \quad k < j. \tag{A.28}$$

Again we firstly consider only the first constraint. The problem is equivalent to the minimization of

$$\widetilde{f}_j \;=\; \frac{1}{2}\langle y_j|(PHP)|y_j\rangle \;-\; \widetilde{\epsilon}_j(\langle y_j|(PSP)|y_j\rangle \;-\; 1). \tag{A.29}$$

The gradient $|g_j\rangle$ is now given by

$$|g_j\rangle \;=\; (PHP)|y_j\rangle \;-\; \widetilde{\epsilon}_j(PSP)|y_j\rangle \tag{A.30}$$

where

$$\widetilde{\epsilon}_j \;=\; \frac{\langle y_j|(PSP)(PHP)|y_j\rangle}{\langle y_j|(PSP)^2|y_j\rangle} \tag{A.31}$$

ensures that

$$\langle g_j|(PSP)|y_j\rangle \;=\; 0. \tag{A.32}$$

Now we have to care about the second set of constraints. We want that

$$\langle g_j|PS|\psi_k\rangle \;=\; 0. \tag{A.33}$$

And again this is obtained by orthogonalizing, with the overlap matrix S, $|Pg_j\rangle$ to $|\psi_k\rangle, k < j$:

$$|Pg_j^0\rangle \;=\; |Pg_j^0\rangle \;-\; \sum_{k<j}\langle g_j^0|PS|\psi_k\rangle|\psi_k\rangle. \tag{A.34}$$

Modified preconditioned algorithm

Starting from an initial guess $|\psi_j^0\rangle$ (where $\langle\psi_k|S|\psi_j^0\rangle = 0$, $\langle\psi_j^0|S|\psi_j^0\rangle = 1$), one searches for new vector as:

$$|\psi_j^n(\theta)\rangle \;=\; \cos\theta|\psi_j^{n-1}\rangle \;+\; \sum_{i=1}^{N}\theta|P\tilde{h}_j^{n-1}\rangle \tag{A.35}$$

where

$$|P\tilde{h}_j^n\rangle \;=\; \frac{|Ph_j^n\rangle}{\langle Ph_j^n|S|Ph_j^n\rangle^{1/2}} \tag{A.36}$$

and $|Ph_j^n\rangle$ is the conjugate gradient. We define

$$|Pu_j^n\rangle \;=\; |Pg_j^n\rangle \;+\; \gamma_j^{n-1}|Ph_j^{n-1}\rangle, \tag{A.37}$$

$$\gamma_j^{n-1} \;=\; \frac{\langle Pg_j^n|P^{-2}S|Pg_j^n\rangle}{\langle Pg_j^{n-1}|P^{-2}S|Pg_j^{n-1}\rangle} \simeq \frac{\langle Pg_j^n - Pg_j^{n-1}|P^{-2}S|Pg_j^n\rangle}{\langle Pg_j^{n-1}|P^{-2}S|Pg_j^{n-1}\rangle} \tag{A.38}$$

with $\gamma_j^{-1} = 0$. The gradient $|Pg_j^n\rangle$ is given by

$$|Pg_j^n\rangle \;=\; P^2H|\psi_j^n\rangle \;-\; \tilde{\epsilon}_j^n SP^2|\psi_j^n\rangle \;-\; \sum_{k<j}\lambda_{jk}^n|\psi_k\rangle \tag{A.39}$$

where

$$\lambda_{jk}^n \;=\; \langle\psi_k|S(P^2H \;-\; \tilde{\epsilon}_j^n SP^2)|\psi_j^n\rangle, \qquad \tilde{\epsilon}_j^n \;=\; \frac{\langle\psi_j^n|SP^2H|\psi_j^n\rangle}{\langle\psi_j^n|S^2P^2|\psi_j^n\rangle} \tag{A.40}$$

$|Pu_j^n\rangle$ is by construction orthogonal to $|\psi_k\rangle$ but not to $|\psi_j^n\rangle$:

$$\beta_j^n \;=\; \langle Pu_j^n|S|\psi_j^n\rangle \;=\; \gamma_j^{n-1}\langle Ph_j^{n-1}|S|\psi_j^n\rangle \;=\; \gamma_j^{n-1}\sum_{i=1}^{N}\theta_j^{n-1}\langle Ph_j^{n-1}|S|Ph_j^{n-1}\rangle \neq 0. \tag{A.41}$$

One gets the conjugate direction $|Ph_j^n\rangle$ from

$$|Ph_j^n\rangle \;=\; |Pu_j^n\rangle \;-\; \beta_j^n|\psi_j^n\rangle. \tag{A.42}$$

Note that only P^2 (or P^{-2}) is actually used.

A.2 Parallel diagonalization

For the particular case of real symmetric matrices we have used a parallel diagonalization algorithm, the *parallel Jacobi method* [75]. Basically, the Jacobi idea is to systematically reduce the "norm" of the off-diagonal elements of the matrix,

$$off(A) = \sqrt{\sum_{i=1}^{n}\sum_{\substack{j=1\\ j\neq i}}^{n} a_{ij}^2}\ , \tag{A.43}$$

this is done using the rotation matrix

$$J(p,q) = \begin{array}{cc} \begin{pmatrix} 1 & \cdots & 0 & \cdots & 0 & \cdots & 0 \\ \vdots & \ddots & \vdots & & \vdots & & \vdots \\ 0 & \cdots & c & \cdots & s & \cdots & 0 \\ \vdots & & \vdots & \ddots & \vdots & & \vdots \\ 0 & \cdots & -s & \cdots & c & \cdots & 0 \\ \vdots & & \vdots & & \vdots & \ddots & \vdots \\ 0 & \cdots & 0 & \cdots & 0 & \cdots & 1 \end{pmatrix} & \begin{array}{c} \\ \\ \leftarrow\ p \\ \\ \leftarrow\ q \\ \\ \\ \end{array} \\ \begin{array}{ccccccc} & & \uparrow & & \uparrow & & \\ & & p & & q & & \end{array} & \end{array} \tag{A.44}$$

which we call *Jacobi rotation.* c and s are chosen in such a way that

$$\begin{pmatrix} c & s \\ -s & c \end{pmatrix}^T \begin{pmatrix} a_{pp} & a_{pq} \\ a_{qp} & a_{qq} \end{pmatrix} \begin{pmatrix} c & s \\ -s & c \end{pmatrix} = \begin{pmatrix} b_{pp} & 0 \\ 0 & b_{qq} \end{pmatrix}. \tag{A.45}$$

The matrix $B = J^TAJ$ is identical to A except for the rows and columns p and q. It is easy to show that $off(B)^2 = off(A)^2 - 2a_{pq}^2$. Choosing (p,q) in all the possible way is what we call a *sweep*. One *sweep* is not enough to diagonalize the matrix, since an element in the position say $(\bar{p}, \bar{q})$ set to zero by applying $J(\bar{p}, \bar{q})$ is in general put again to a number different from zero by applying a rotation $J(p', \bar{q})$ for example. However, every *sweep* reduces the sum of the off diagonal elements of A hence, by applying a sufficient number of sweeps, the matrix is diagonalized within an arbitrary precision (see Ref. [75] for a discussion). This algorithm is generally inferior as compared to other diagonalization methods, such as the QR algorithm, but it can be solved in parallel on a ring of processors (PE's). Moreover, if the matrix is already almost diagonal the Jacobi algorithm can take advantage of it, QR no.

The idea to solve the problem on a ring of PE's is the following. Each *sweep* if formed by $N = n(n-1)/2$ Jacobi rotations, where n is the dimension of the matrix. For the moment let us suppose n an even number. Among all the possible N rotations it is always possible to chose $n/2$ of them which are independent, i.e. applied to $n/2$ not overlapping couples of indices. We call a *sub-sweep* each of the possible $(n-1)$ choices of $n/2$ independent rotations. Now, each *sub-sweep* can be divided among a set of (at most) $n/2$ different PE's. Moreover, each PE only needs the housing of the columns of the matrix A corresponding to the partial part of the *sub-sweep* which must be solved on it. Example: suppose $n = 4$ and 2 PE's. There are 3 possible *sub-sweeps*,
(1,2)(3,4); (1,4)(2,3); (1,3)(2,4);
for the first *sub-sweep* PE 1 houses the columns $(1, 2)$ and PE 2 the columns $(3, 4)$. PE 1 calculates $J(1, 2)$ and makes the product $AJ(1, 2)$, while PE 2 calculates $J(3, 4)$ and makes the product $AJ(3, 4)$. Note that PE 1 only needs columns 1 and 2 to perform the product, while PE 2 only columns 3 and 4. Then PE 1 sends $J(1, 2)$ to PE 2 and receives from PE 2 $J(3, 4)$. Now both PE's can calculate $J^T AJ$ and the first *sub-sweep* is completed. Before starting the second *sub-sweep*, column 2 is send from PE 1 to PE 2 and column 4 from PE 2 to PE 1 and the algorithm is repeated. Finally, column 4 is send from PE 1 to PE 2 and column 3 from PE 2 to

PE 1 and the last *sub-sweep* is performed. In the general case one has n columns and p PE's, with $n/2 \geq p$ and the algorithm is implemented in the following way:

Starting configuration:

$$\underbrace{\left|\begin{array}{cccc} 1 & 3 & \cdots & \frac{n}{p}-1 \\ 2 & 4 & \cdots & \frac{n}{p} \end{array}\right|}_{\text{PE 1}}\underbrace{\left|\begin{array}{ccc} \frac{n}{p}+1 & \cdots & \frac{2n}{p}-1 \\ \frac{n}{p}+2 & \cdots & \frac{2n}{p} \end{array}\right|}_{\text{PE 2}}\cdots\underbrace{\left|\begin{array}{ccc} \frac{(p-1)n}{p}+1 & \cdots & n-1 \\ \frac{(p-1)n}{p}+2 & \cdots & n \end{array}\right|}_{\text{PE p}},$$

the couples that define the Jacobi rotations are the columns of the matrices above, for example the first PE houses the first n/p columns and applies the Jacobi rotations for the couples $(1,2),(3,4),\cdots(\frac{n}{p}-1,\frac{n}{p})$. Each PE calculates its own part of the matrix J and sends it to all the other PE's. Once it has in its own memory all the matrix J, it can compute J^TAJ, concluding the *sub-sweep*.

Following steps:

$$\underbrace{\left|\begin{array}{ccccccc} 1 & & 3 & \rightarrow & \cdots & \rightarrow & \frac{n}{p}-1 \\ & \nearrow & & & & & \\ 2 & \leftarrow & 4 & \leftarrow & \cdots & \leftarrow & \frac{n}{p} \end{array}\right|}_{\text{PE 1}} \begin{array}{c} \Rightarrow \\ \\ \Leftarrow \end{array} \underbrace{\left|\begin{array}{ccccc} \frac{n}{p}+1 & \rightarrow & \cdots & \rightarrow & \frac{2n}{p}-1 \\ & & & & \\ \frac{n}{p}+2 & \leftarrow & \cdots & \leftarrow & \frac{2n}{p} \end{array}\right|}_{\text{PE 2}} \begin{array}{c} \Rightarrow \\ \cdots \\ \Leftarrow \end{array}$$

$$\cdots \begin{array}{c} \Rightarrow \\ \\ \Leftarrow \end{array} \underbrace{\left|\begin{array}{ccccc} \frac{(p-1)n}{p}+1 & \rightarrow & \cdots & \rightarrow & n-1 \\ & & & & \downarrow \\ \frac{(p-1)n}{p}+2 & \leftarrow & \cdots & \leftarrow & n \end{array}\right|}_{\text{PE p}},$$

where with the symbols $(\rightarrow,\leftarrow)$ we indicate the logical movements of the columns within each PE, while with $(\Rightarrow,\Leftarrow)$ we refer to physical columns exchange. After $(n-1)$ steps the *sweep* is completed and one can check the quantity $off(A)$ defined above by summing the squares of the off-diagonal terms of the matrix A on each PE and then summing the partial results. Once $off(A)$ is "zero" within the machine precision the diagonalization is done. Accumulating the rotation matrices J one also

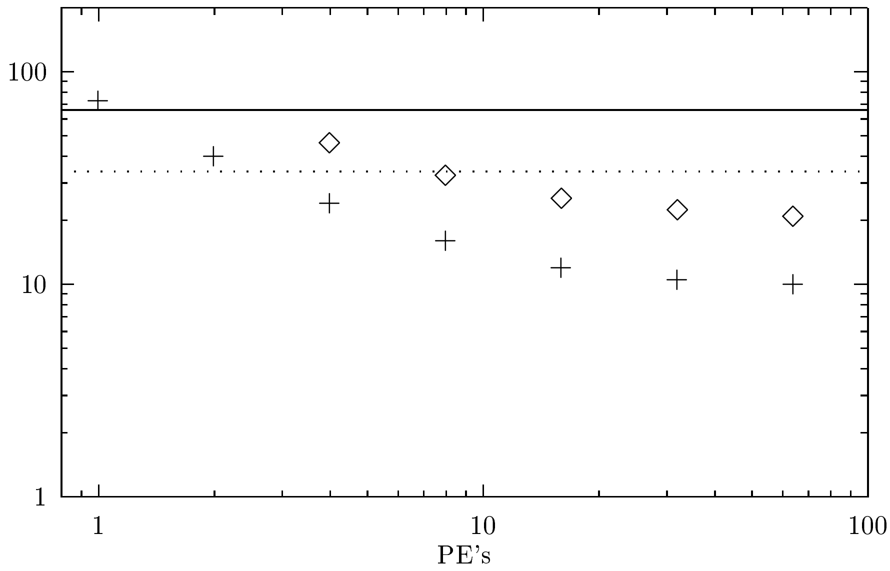

(a) $N_{band} = 122$

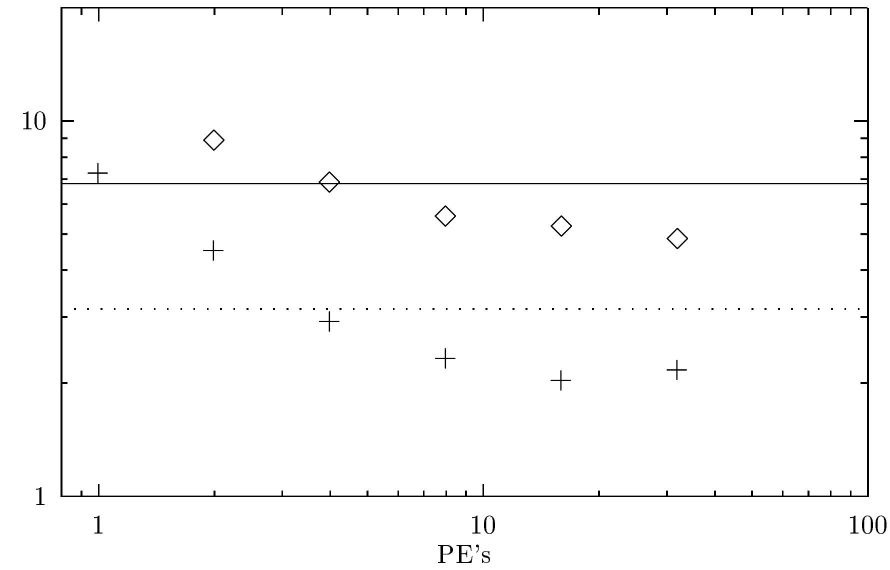

(b) $N_{band} = 61$

Figure A.1: Diagonalization time (in seconds) as a function of the number of PE's on the Cray-T3D (diamonds) and Cray-T3E (crosses) machines for the first iteration of (a) the Rh(001)-(2×2)p4g structure (122 bands) and (b) the Rh(001)-(2×2) structure (61 bands). The QR serial time is also displayed for the Cray-T3D (full line) and Cray-T3E (dotted line).

has the eigenvectors of the matrix A. The method is designed to work only for even n, however the extension to odd n is straightforward, for example it is sufficient to add a row and a column of zeros to A and set the element a_{n+1n+1} equal to a big number (BN), larger then the largest eigenvalue of A. Then, once A is diagonalized, one simply forget about the largest eigenvalue (which is BN) and its corresponding eigenvector.

In Fig. A.1 we report the diagonalization time as a function of the number of PE's on a Cray-T3D and Cray/T3E machines for the first scf iteration of two selected problems, and a comparison with a standard serial QR diagonalization. The method become more and more convenient as the dimension of the matrix is larger and larger. The dimension of the matrices go from N_{band} to DN_{band}, where in these case $D = 4$, in (a) $N_{band} = 122$ and in (b) $N_{band} = 61$.

Appendix B

Constrained minimization

Optimizing the structure of a system under external constraints is a problem of general interest. In section 2.3, for instance, it has been useful to find the energy of 1 ML of CO adsorbed on Rh(110) as a function of the tilt angle of the molecular axis with respect to the surface normal. More generally, one is often interested to know the energy of a system as a function of a collective coordinate, such as a reaction coordinate in a chemical reaction. In all these cases the constraint is *holonomic*, i.e. there is a *constraint equation* which reduces the number of degrees of freedom of the system from $3 \times N_{at}$ to $3 \times N_{at} - 1$,

$$G(\mathbf{x}) = 0, \tag{B.1}$$

where $\mathbf{x}$ is a variable in a $3 \times N_{at}$ dimensions space and describes the space configuration of the system, N_{at} is the number of atoms.

The constraint equation B.1 defines an hyper-surface in the configuration space. Suppose that at the initial step $\mathbf{x_0}$ the constraint equation is satisfied, i.e. $G(\mathbf{x_0}) = 0$, we want to move the atoms to a new position $\mathbf{x_1}$, such that the energy is decreased and the constraint equation is satisfied: $E(\mathbf{x_1}) < E(\mathbf{x_0}); G(\mathbf{x_1}) = 0$. One recipe to achieve the latter result is the following:

- we move the atoms in such a way that the components of the displacements which are orthogonal to the hyper-surface are zero.

- we refine the move so as to satisfy exactly eq. B.1

To this end we modify the forces acting on the atoms in the following way:

$$\mathbf{F}' = \mathbf{F} + \lambda \nabla G, \tag{B.2}$$

with

$$\lambda = -\frac{\mathbf{F} \cdot \nabla G}{|\nabla G|^2}, \tag{B.3}$$

where $\mathbf{F}$ is the "free" force and $\mathbf{F}'$ is the constrained one. In this way $\nabla G \cdot \mathbf{F}' = 0$, i.e. the force component orthogonal to the hyper-surface is zero. Now we construct

$$\delta \mathbf{x} = \underline{\underline{\mathrm{A}}} \cdot \mathbf{F}', \tag{B.4}$$

where $\underline{\underline{\mathrm{A}}}$ may be simply proportional to the identity matrix, or, in a smart minimization scheme, it is a suitable preconditioning matrix which exploits the partial knowledge of the Hessian accumulated during the minimization procedure. [76]. Using $\delta\mathbf{x}$ we construct $\mathbf{x_1^*} = \mathbf{x_0} + \delta\mathbf{x}$. We write $\mathbf{x_1^*}$ instead of $\mathbf{x_1}$ because in general $G(\mathbf{x_1^*}) \neq 0$. This happens if the step $\delta\mathbf{x}$ is too large with respect to the curvature of the hyper-surface. In this case we need to perform the second step of the recipe: if the step $\delta\mathbf{x}$ is not too big we can write:

$$G(\mathbf{x_1}) = G(\mathbf{x_1^*}) + (\mathbf{x_1} - \mathbf{x_1^*}) \cdot \nabla G|_{\mathbf{x}=\mathbf{x_1^*}} = 0, \tag{B.5}$$

and assuming that, in first approximation

$$(\mathbf{x_1} - \mathbf{x_1^*}) = \alpha \nabla G|_{\mathbf{x}=\mathbf{x_1^*}}, \tag{B.6}$$

we have

$$\alpha = -\frac{G(\mathbf{x_1^*})}{|\nabla G|_{\mathbf{x}=\mathbf{x_1^*}}|^2}, \tag{B.7}$$

and then we construct

$$\mathbf{x_1^{**}} = \mathbf{x_1^*} - \frac{G(\mathbf{x_1^*})}{|\nabla G|_{\mathbf{x}=\mathbf{x_1^*}}|^2} \cdot \nabla G|_{\mathbf{x}=\mathbf{x_1^*}}, \tag{B.8}$$

and check if $G(\mathbf{x_1^{**}}) = 0$. In out case we needed to iterate the procedure at most for a couple of times.

Appendix C

Molecular dynamics

Our implementation of molecular dynamics is based on the traditional self-consistent scheme described in the first chapter and in the Appendix A, i.e. we bring the electrons to the BO surface at each step. This technique can be very costly, since the self-consistency required in the KS equation must be high in order to calculate good forces. Therefore, once the KS equation is solved for a particular ionic configuration, which is a step of the dynamical simulation, it is fundamental to have a good algorithm to extrapolate the starting configuration of the next step, so that the number of self-consistency cycles is as small as possible. In our algorithm we extrapolate the potential. We have tried two potential extrapolation schemes. In the first one, the new potential is calculated from an extrapolated charge density, which is simply approximated by the charge density of the previous step plus the difference between the atomic charge density of the new ions configuration and the old one (NOACD). In the second case, we have used the multi-linear extrapolation

$$V(t_n) = \sum_{m=1}^{M} (-1)^{m+1} \begin{pmatrix} M \\ m \end{pmatrix} V(t_{n-m}), \tag{C.1}$$

for different values of M. A comparison between the NOACD extrapolation scheme and the Multi-linear one for various values of M is displayed in Fig. C.1. for a system of 64 silicon atoms. The starting configuration is the bulk equilibrium one and the starting temperature is 300°K. The time step is 135 a.u., corresponding to

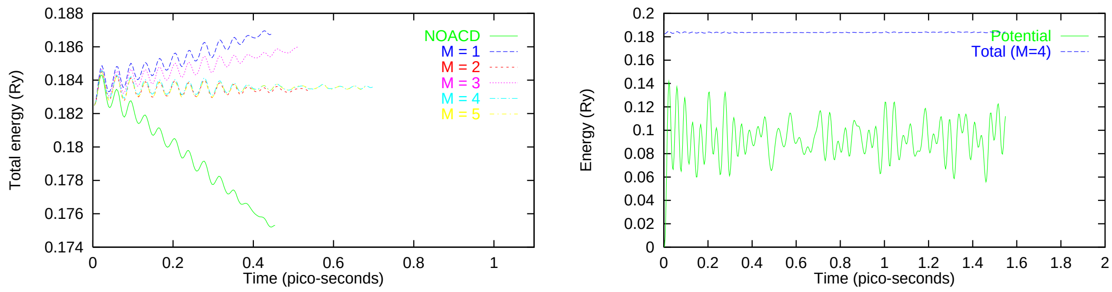

(a) Total energy (constant of motion) (b) Potential energy and constant of motion

Figure C.1: (Color) Total energy (constant of motion) and potential energy as a function of time for a molecular dynamics run of 64 silicon atoms at $\approx 150^{o}$K.

3.267 femto-seconds, which is 1/20 of the optical phonon frequency. The CPU time is not much different among the different schemes used (see Table C.1), with besides the $M = 1$ case which corresponds to no extrapolation at all. What is somewhat different is the conservation of the total energy, which is worse in the NOACD case. This fact reflects an important technical problem. Force calculation is a particularly delicate problem. In order to have a good accuracy it is necessary to have a highly converged KS wave-functions. The drift in the total energy is due to the fact that the lack in self-consistency for the KS orbitals is always in the same direction in a dynamical simulation, this results in a sort of 'friction' for the system which therefore does not conserve its total energy. It is not a real friction since the total energy drift can be positive or negative. In the NOACD scheme the difference between the self-consistent charge and the sum of the atomic one is left always 'behind', and this fact results maybe in a higher systematic error in the lack of self-consistency.

Extrapolation algorithm	NOACD	$M = 1$	$M = 2$	$M = 3$	$M = 4$	$M = 5$
CPU time/ps (hours)	32	62	39	31	32	37

Table C.1: CPU time (in hours) per pico-second on a IBM-595 machine for the same system using different extrapolation algorithms for the starting potential. In all cases the time is about one half of that taken when no extrapolation is performed ($M = 1$).

Acknowledgments

I want to thank Alessandro Baraldi, Giovanni Comelli, Giorgio Paolucci, Maya Kiskinova and Renzo Rosei for very useful discussions and suggestions, and for inspiring the work of this thesis. I am grateful to Stefano Serra for providing us with its spin-polarized code. Thanks to Paolo Giannozzi, for its continuous help in the computational problems. Thanks to Sandro Scandolo and Guido Chiarotti, for helpful and stimulating discussions. A special thanks to Stefano de Gironcoli, for its continuous suggestions and critical discussions.

Finally, I want to thank Stefano Baroni, who taught me most of the things I used to complete the work of this thesis.

Bibliography

[1] For an introduction on surface physics see for example: A. Zangwill, *Physics at surfaces*, Cambridge University Press, 1988.

[2] For a review on surface catalysis see for example: G. A. Somorjai, *Introduction to surface chemistry and catalysis*, John Wiley & Sons, New York, 1994.

[3] B.H. Bransden and C.J. Joachain *Physics of atoms and molecules*, pag. 393, Longman Scientific & Technical, 1983.

[4] M. Garofalo, E.Tosatti, and F. Ercolessi, Surf. Sci. **188**, 321 (1987).

[5] S.P. Chen and A.F. Voter, Surf. Sci. **244**, L107 (1991).

[6] V.R. Dhanak, G. Comelli, G. Cautero, G. Paolucci, M. Kiskinova, K.C. Prince and R. Rosei, Chem. Phys. Lett. **188**, 237 (1992).

[7] G. Comelli, V.R. Dhanak, M. Kiskinova, N. Pangher, G. Paolucci, K.C. Prince and R. Rosei, Surf. Sci. **260**, 7 (1992); *ibid.* **269/270**, 360 (1992).

[8] D. Alfè, P. Rudolf, M. Kiskinova, and R. Rosei, Chem. Phys. Lett. **211**, 220 (1993).

[9] R.G. Parr and W. Yang *Density-Functional Theory of Atoms and Molecules*, Oxford Science Publications, 1989.

[10] R.M. Dreizler and E.K.U. Gross *Density Functional Theory*, Springer-Verlag, 1990.

[11] W. E. Pickett, *Computer Phys. Reports* **9**, 115 (1989).

[12] A. Baraldi, G. Comelli, G. Paolucci, M. Kiskinova and R. Rosei.

[13] M. Bowker, Q. Guo and R. Joyner, Surf. Sci. **253**, 33 (1991).

[14] V. Schmatloch and N.Kruse Surf. Sci. **269/270**, 488 (1992).

[15] A. Baraldi, V.R. Dhanak, G. Comelli, K.C. Prince and R. Rosei, Surf. Sci. **293**, 246 (1993).

[16] V.R. Dhanak, A. Baraldi, G. Comelli, G. Paolucci, M. Kiskinova, and R. Rosei, Surf. Sci. **295**, 287 (1993).

[17] L. Casalis, A. Baraldi, G. Comelli, V.R. Dhanak, M. Kiskinova, R. Rosei, Surf. Sci. **306**, 193 (1994).

[18] J.D. Batteas, A. Barbieri, E.K. Starkey, M.A. Van Hove, G.A. Somorjai, Surf. Sci. **313**, 341 (1994).

[19] J.J. Weimer, J. Loboda-Cackovic, J.H. Block, Surf. Sci. **316**, 123 (1994).

[20] K.C. Prince, A. Santoni, A. Morgante, G. Comelli, Surf. Sci. **317**, 397 (1994).

[21] R. Gómez, A. Rodes, J.M. Péres, J.M. Feliu, A. Aldaz, Surf. Sci. **327**, 202 (1995).

[22] C.M. Comrie and R.M. Lambert, *J. Chem. Soc. Faraday Trans.* **I 72**, 1659 (1976).

[23] H.H. Madden, J. Kuppers and G. Ertl, J. Chem. Phys. **58**, 3401 (1973).

[24] G. Ertl and P. Rau, Surf. Sci. **15**, 443 (1969).

[25] K. Christmann and G. Ertl, *Z. Naturfosh.* **28a**, 1144 (1973).

[26] D.J. Hannaman and M.A. Passler, Surf. Sci. **203**, 449 (1988).

[27] A. Wander, P. Hu and D.A. King, Chem. Phys. Lett. **201**, 393 (1993).

[28] J.R. Mercer, P. Finetti, F. M. Leibsle, R. McGrath, V.R. Dhanak, A. Baraldi, K.C. Prince, R. Rosei, Surf. Sci. **352-354**, 173 (1996); J.R. Mercer, P. Finetti, M. J. Scantlebury, U. Beierlein, V.R. Dhanak, and R. McGrath, Phys. Rev. B **55** (1997).

[29] W. Daum, S.Lehwald and H. Ibach, Surf. Sci. **178**, 528 (1986).

[30] C. Klink, L. Olesen, F. Besenbacher, I. Stensgaard, E. Laegsgaard, N. D. Lang Phys. Rev. Lett. **71**, 4350 (1993).

[31] F. M. Leibsle, Surf. Sci. **297**, 98 (1993).

[32] J. H. Onuferko, D.P. Woodruff and B. W. Holland, Surf. Sci. **87**, 357 (1979).

[33] L. Wenzel, D. Arvanitis, W. Daum, H.H. Rotermund, J. Stohr, K. Baberschke, H. Ibach Phys. Rev. B **36**, 7689 (1987).

[34] P. Hohenberg and W. Kohn, Phys. Rev. **136**, B864 (1964).

[35] W. Kohn and L. Sham, Phys. Rev. **140**, A1133 (1965).

[36] E. R. Davidson, J. Comput. Phys. **17**, 87 (1975).

[37] D. Ceperley and B. Alder, Phys. Rev. Lett. **45**, 566 (1980).

[38] J. P. Perdew and A. Zunger, Phys. Rev. B **23**, 5040 (1981).

[39] N.W. Ashcroft and N.D. Mermin, *Solid State Physics*, Holt, Rinehart and Wiston, 1976.

[40] A. Baldereschi, Phys. Rev. B **7**, 5212 (1973).

[41] D. J. Chadi, and M. L. Cohen, Phys. Rev. B **8**, 5747 (1973).

[42] H. J. Monkhorst and J. D. Pack, Phys. Rev. B **13**, 5188 (1976). See also D. J. Chadi, Phys. Rev. B **16**, 1746 (1977) and J. D. Pack and H. J. Monkhorst Phys. Rev. B **16**, 1748 (1977) for a discussion on the particular case of *hexagonal* Bravais lattices.

[43] C. L. Fu, and K. M. Ho, Phys. Rev. B **28**, 5480 (1983).

[44] M. Methfessel and A. Paxton, Phys. Rev. B **40**, 3616 (1989).

[45] D. R. Hamann, M. Schlüter and C. Chiang, Phys. Rev. Lett. **43**, 1494 (1979).

[46] G. P. Kerker, *J. Phys. C* **13**, L189 (1980).

[47] G. B. Bachelet, D. R. Hamann, and M. Schlüter Phys. Rev. B **26**, 4199 (1982).

[48] L. Kleinman and D.M. Bylander, Phys. Rev. Lett. **48**, 1425 (1982).

[49] X. Gonze, P. Käckell, and M. Scheffler, Phys. Rev. B **41**, 12264 (1990).

[50] D. Vanderbilt, Phys. Rev. B **41**, 7892 (1990).

[51] H. Hellmann, Einführung in die Quantenchemie (Deuticke, Leipzig, 1937); R. P. Feynmann, Phys. Rev. **56**, 340 (1939).

[52] K. Stokbro, Phys. Rev. B **53**, 6869 (1996).

[53] K. Stokbro and S. Baroni, Surf. Sci., **370**, 166 (1997).

[54] `http://www.shef.ac.uk/ chem/web-elements/`.

[55] K. Laasonen, A. Pasquarello, R. Car, C. Lee, D. Vanderbilt, Phys. Rev. B **47**, 10142 (1993).

[56] D. Alfè and S. Baroni, Surf. Sci. **382**, L666 (1997); D. Alfè, S. de Gironcoli, S. Baroni, *submitted.*

[57] W. Nichtl, N. Bickel, L. Hammer, K. Heinz and K. Müller, Surf. Sci. **188**, L729 (1987).

[58] C. Comicioli, *Master Thesis* (University of Trieste, Italy, 1991).

[59] A.M. Begley, S.K. Kim, F. Jona, and P.M. Marcus, Phys. Rev. B **48**, 12326 (1993).

[60] *CRC Handbook of Chemestry and Physics*, 67th ed. (1987), p. E-89.

[61] L.Z. Mezey and J.Giber, *Jpn J. Appl. Phys.* **21**, 1569 (1982).

[62] P. J. Feibelmann and D. R. Hamann, Surf. Sci. **234**, 377 (1990); M. Methfessel, D. Hennig, and M. Scheffler, Phys. Rev. B **46**, 4816 (1992); I. Morrison, D. M. Bylander, and L. Kleinmann, Phys. Rev. Lett. **71**, 1083 (1993); J.-H. Cho and M.-H. Kang, Phys. Rev. B Lett. **52**, 13805 (1995).

[63] A. Eichler, J. Hafner, J. Furthmüller, G. Kresse, Surf. Sci. **346**, 300 (1996).

[64] J. H. Cho and M. Scheffler Phys. Rev. Lett. **78**, 1299 (1997).

[65] W. Nichtl, N.Bickel, L.Hammer, K. Heinz, and K. M*ü*ller, Surf. Sci. **188**, L729 (1987).

[66] J.W.D. Connoly and A.R. Williams, Phys. Rev. B **27**, 5169 (1983).

[67] David Chandler, *Introduction to modern statistical mechanics* Oxford University Press, Oxford, 1987.

[68] L. Verlet Phis. Rev **159**, 98-103 (1967).

[69] W. Oed, B. Dötsch, L. Hammer, K. Heinz, and K. Müller, Surf. Sci. **207**, 55 (1988).

[70] K. Heinz, W. Oed, J. B. Pendry, Phys. Rev. B **41**, 10179 (1990); W. Oed, H. Lindner, U. Starke, K. Heinz, K. Müller, D. K. Saldin, P. de Andres, J.B. Pendry, Surf. Sci. **225**, 242 (1990); W. Oed, U. Starke, K. Heinz, K. Müller, J. Phys. Condens. Matter, **3**, s223 (1991); W. Oed, H. Lindner, U. Starke, K. Heinz, K. Müller, Surf. Sci. **224**, 195 (1989).

[71] E. Kopatzki and R.J. Behm, Surf. Sci. **245**, 255 (1991).

[72] T. Sazaki, A. M. Rappe, and S. G. Louie, Phys. Rev. B **52**, 12760 (1995).

[73] J. Tersoff and D. R. Hamann, Phys. Rev. B **31**, 805 (1985).

[74] M. Bernasconi, G. L. Chiarotti, and E. Tosatti, Phys. Rev. B **52**, 9999 (1995).

[75] G. H. Golub, C. F. Van Loan, *Matrix computation*, second edition, The Johns Hopkings University Press, Baltimore at London, 1989.

[76] Broyden-Fletcher-Goldfarb-Shanno (BFGS) algorithm, it can be found in *Numerical Recipies, The art of scientific computing* Cambridge University Press, 1986.